3-D Snake Robot Motion: Nonsmooth Modeling, Simulations, and Experiments

Aksel A. Transeth, *Member, IEEE*, Remco I. Leine, Christoph Glocker, and Kristin Y. Pettersen, *Senior Member, IEEE*

***Abstract*—A nonsmooth (hybrid) 3-D mathematical model of a snake robot (without wheels) is developed and experimentally validated in this paper. The model is based on the framework of nonsmooth dynamics and convex analysis that allows us to easily and systematically incorporate unilateral contact forces (i.e., between the snake robot and the ground surface) and friction forces based on Coulomb's law of dry friction. Conventional numerical solvers cannot be employed directly due to set-valued force laws and possible instantaneous velocity changes. Therefore, we show how to implement the model for numerical treatment with a numerical integrator called the time-stepping method. This method helps to avoid explicit changes between equations during simulation even though the system is hybrid. Simulation results for the serpentine motion pattern lateral undulation and sidewinding are presented. In addition, experiments are performed with the snake robot "Aiko" for locomotion by lateral undulation and sidewinding, both with isotropic friction. For these cases, back-to-back comparisons between numerical results and experimental results are given.**

***Index Terms*—3-D snake robot, kinematics, nonsmooth dynamics, time-stepping method.**

I. Introduction

WHEELED mechanisms constitute the backbone of most ground-based means of transportation. Unfortunately, rough terrain makes it hard, if not impossible, for such mechanisms to move. To be able to move in various terrains, such as going through narrow passages and climb on rough ground, the high-mobility property of snakes is recreated in robots that look and move like snakes.

Snake robots most often have a high number of DOFs, and they are able to move forward without using active wheels or legs. Due to the high number of DOF, it can be quite expensive and time-consuming to build and maintain a snake robot. This motivates the development of accurate mathematical models of snake robots. Such models can be used for synthesis and testing of various serpentine motion patterns intended for serpentine locomotion.

Manuscript received July 19, 2007; revised November 29, 2007. This paper was recommended for publication by Associate Editor S. Ma and Editor F. Park upon evaluation of the reviewers' comments.

A. A. Transeth is with the Department of Applied Cybernetics, SINTEF Information and Communication Technology (ICT), NO-7465 Trondheim, Norway (e-mail: aksel.transeth@sintef.no).

R. I. Leine and Ch. Glocker are with the Institut für Mechanische Systeme (IMES) Centre of Mechanics, Eidgenössische Technische Hochschule (ETH) Zürich, CH-8092 Zurich, Switzerland (e-mail: remco.leine@imes.mavt.ethz.ch; christoph.glocker@imes.mavt.ethz.ch).

K. Y. Pettersen is with the Department of Engineering Cybernetics, Norwegian University of Science and Technology, NO-7491 Trondheim, Norway (e-mail: kristin.y.pettersen@itk.ntnu.no).

Color versions of one or more of the figures in this paper are available online at http://ieeexplore.ieee.org.

Digital Object Identifier 10.1109/TRO.2008.917003

The first working snake robot was built in 1972 [1]. This robot was limited to planar motion, but snake robots capable of 3-D motion have appeared more recently [2]–[6]. Together with the robots, mathematical models of both the kinematics and the dynamics of snake robots have also been developed. Purely kinematic 3-D models have been presented in [6]–[8], where frictional contact between the snake robot and the ground is not included in the model. Hence, contact between the snake robot and the ground surface is either modeled with frictionless passive wheels, or the parts of the snake robot that touches the ground are defined as anchored to the ground [9]. A model of the dynamics of motion is needed to describe the friction forces a snake robot without wheels is subjected to when moving over a surface. Most mathematical models that describe the dynamics of snake robot motion have been limited to planar (2-D) motion [10]–[13], and 3-D mathematical models of snake robots have only recently been developed [3], [7]. 3-D models facilitate testing and development of 3-D serpentine motion patterns such as sinus lifting and sidewinding. A description of these motion patterns is found in, e.g., [4]. A physics engine called the open dynamics engine (ODE) has been employed to simulate a 15-link snake robot instead of deriving explicit expressions for its dynamics in [14]. Such software makes it easy to change the geometry of a snake robot if needed, and the time needed to prepare a working model is relatively short [15].

On a flat surface, the ability of a snake robot to move forward is dependent on the friction between the ground surface and the body of the snake robot. Hence, unilateral contact forces and friction forces are important parts of the mathematical model of a snake robot. The friction forces have usually been based on a Coulomb or viscous-like friction model [11], [12], and Coulomb friction has most often been modeled using a sign function [12], [16]. The contact between a snake robot and the ground surface can sometimes be approximated by a no-sideways-slip constraint for snake robot with wheels [17], [18]. However, such an approximation is not valid for wheel-less snake robots. The unilateral contact forces have been modeled as a mass-spring-damper system in [3] (i.e., compliant contact), and each link has only a single and fixed contact point with the ground surface. When running simulations, direct implementations or approximations of the sign function can lead to an erroneous description of sticking contacts or very stiff differential equations. Also, a mass-spring-damper model introduces a very stiff spring that leads to stiff differential equations. In addition, it is not clear how to determine the dissipation parameters of the contact unambiguously when using a compliant model [19]. The ODE implements a form of rigid body contact (i.e., not compliant contact). However, the implementation of this engine trades off

Fig. 1. NTNU/SINTEF snake robot "Aiko."

simulation accuracy in order to increase simulation speed and stability [15], [20].

In this paper, we develop a nonsmooth (hybrid) 3-D mathematical model of a snake robot with cylindrical links without wheels. *Set-valued* force laws for the constitutive description of unilateral contact forces and friction forces in a 3-D setting are described in the framework of nonsmooth dynamics and convex analysis [19], [21], [22]. Moreover, the model has a moving contact point on the *surface* of each link for contact with the ground surface instead of just a fixed point for each link. The latter is an approach employed in prior publications on mathematical models of 3-D snake robot motion. Stick-slip transitions (based on a set-valued Coulomb friction law) and impacts with the ground are modeled as instantaneous transitions. This results in an accurate model of *spatial* Coulomb friction where both the direction of the friction force and a true stick-phase are taken properly into account. For wheel-less snake robots, it is important to describe the frictional contact between the wheel-less snake robot and the ground in an accurate manner, both with respect to stick-slip transitions and the direction of the friction force while sliding along the ground surface. This latter property also distinguishes wheel-less snake robots from, e.g., legged mechanisms that most often try to "stick" to the ground rather than sliding along it. The dynamics of the snake robot is described by an equality of measures, which includes the Newton–Euler equations for the nonimpulsive part of the motion as well as impact equations. A particular choice of coordinates results in an effective way of writing the system equations. The set-valuedness of the force laws allows us to write each constitutive law with a single equation and avoids explicit switching between equations (for example, when a collision between the snake robot and the ground surface occurs) even though this is a hybrid system. This is advantageous since the snake robot links repeatedly collides with the ground surface during, e.g., locomotion by sidewinding. A discretization of the equality of measures gives the so-called time-stepping method (see [22] and references therein) that we use for numerical simulation. The description of the model and the method for numerical integration are presented in this paper in such a way that people who are new to the field of nonsmooth dynamics can use this paper as an introduction to nonsmooth modeling of robot manipulators with impacts and friction. In addition, we present experimental results that validate the mathematical model. To the best of our knowledge, this is the first time such a back-to-back comparison between simulation and experimental results is presented for 3-D snake robot motion. The experiments are performed with the snake robot "Aiko" in Fig. 1 built at the Norwegian University of Science and Technology (NTNU)/SINTEF Advanced Robotics Laboratory.

The paper is organized as follows. A short introduction to the modeling procedure is given in Section II. The kinematics of the snake robot with the ground surface as a unilateral constraint is described in Section III. Then, the groundwork for finding the friction and ground contact forces is laid in Section IV. The nonsmooth dynamics is presented in Section V, while the serpentine motion patterns employed in this paper are described in Section VI. The numerical treatment of the mathematical model is given in Section VII. Simulations and experimental validations are given in Section VIII. Conclusions and suggestions for further research are presented in Section IX.

II. Summary of the Mathematical Model

This section contains a brief outline of how to derive the nonsmooth mathematical model of the snake robot. This preliminary section is meant to motivate and ease the understanding of the forthcoming deduction of the system equations.

The snake robot model consists of n links connected by $n-1$ two-DOF cardan joints (i.e., rotational joints). Let $\boldsymbol{u} \in \mathbb{R}^{6n}$ be a vector containing the translational and rotational velocities of all the links of the snake robot (the structure of the snake robot together with the coordinates and reference frames are described further in Section III). Let the differential measures $\mathrm{d}\boldsymbol{u}$ and $\mathrm{d}t$ be loosely described for now as a "possible differential change" in $\boldsymbol{u}$ and time t, respectively, while a more precise definition is given in Section V. The use of differential measures allows for instantaneous changes in velocities that occur for impacts between the snake robot and the ground surface. The system equations for the snake robot can now be written as

$$\mathbf{M}\,\mathrm{d}\boldsymbol{u} - \boldsymbol{h}\,\mathrm{d}t - \mathrm{d}\boldsymbol{R} = \boldsymbol{\tau}_C\,\mathrm{d}t \tag{1}$$

which is called the *equality of measures* [23], where $\mathbf{M} \in \mathbb{R}^{6n\times 6n}$ is the mass matrix, $\boldsymbol{h} \in \mathbb{R}^{6n}$ consists of the smooth forces, $\boldsymbol{\tau}_C \in \mathbb{R}^{6n}$ contains all the joint actuator torques, and $\mathrm{d}\boldsymbol{R} \in \mathbb{R}^{6n}$ accounts for the normal contact forces/impulses from the ground, the Coulomb friction forces/impulses, and the bilateral constraint forces/impulses in the joints. *Note:* We allow in this paper for *instantaneous* changes in velocities usually associated with collisions. Hence, the (normal contact/friction/constraint) *forces* are not always defined due to the infinite accelerations. In these cases, we have *impulses* instead of forces. The nonsmooth equality of measures (1) allows us to formulate in a uniform manner both the smooth and nonsmooth phases of motion. This is achieved partly by representing the contact forces/impulses as *contact impulse measures*.

A substantial part of the beginning of this paper is devoted to deducting the force measure $\mathrm{d}\boldsymbol{R}$. Hence, let us briefly look at how to derive the contribution of the normal contact impulse measure between the ground and the first link in $\mathrm{d}\boldsymbol{R}$. Let $\mathrm{d}\boldsymbol{R}_1 \in \mathbb{R}^6$ be the sum of contact impulse measures that directly affects link 1 (i.e., the six top elements of $\mathrm{d}\boldsymbol{R}$), then

$$\mathrm{d}\boldsymbol{R}_1 = \boldsymbol{w}_N\,\mathrm{d}P_N + \left\{\begin{array}{l}\text{friction and joint constraint}\\ \text{impulse measures}\end{array}\right\} \tag{2}$$

where $\mathrm{d}P_N \in \mathbb{R}$ is the normal contact impulse measure from the ground on link 1, and $\boldsymbol{w}_N \in \mathbb{R}^6$ is the corresponding

generalized force direction, i.e., a Jacobian (subscripts "j" and "1" are omitted for brevity).

Let $g_N \in \mathbb{R}$ be a function giving the shortest distance between the rear part of link 1 and the ground. Such a function is called a *gap function* [24]. The gap function is the starting point for the systematic approach of finding the impulse measures. The ground and the rear part of the link are separated if $g_N > 0$, are in contact if $g_N = 0$, and are penetrating each other if $g_N < 0$. Now, the relative velocity between link 1 and the ground along the shortest line between the two objects can be defined as

$$\gamma_N := \boldsymbol{w}_N^{\mathrm{T}} \boldsymbol{u}_1 \tag{3}$$

where $\boldsymbol{u}_1$ is the velocity of link 1 and $\boldsymbol{w}_N = \partial g_N / \partial \boldsymbol{q}$ is the generalized force direction used in (2). It holds that $\gamma_N = \dot{g}_N$ for almost all t. The normal contact impulse measure $\mathrm{d}P_N$ is related to the relative velocity γ_N through a *set-valued force law* (see Section V-B1. The set-valuedness of the force laws allows us to write each constitutive law (force law) with a single equation and avoids explicit switching between equations (for example, when a collision occurs). In addition, this formulation provides an accurate description of the planar Coulomb friction (see Section V-B2). In the following three sections, we will elaborate on how to derive the elements that constitute (1), that is, the various gap functions, relative velocities, and finally, the forces/impulses that appear in the equality of measures.

III. Kinematics

The kinematics describes the geometrical aspect of motion. From the geometry of the snake robot, we develop *gap functions* for ground contact detection. These functions are also needed for calculating the directions of the contact forces.

This section will first give an overview of the coordinates used to describe the position and orientation of the snake robot. Subsequently, the gap functions will be presented.

A. Coordinates and Reference Frames

The snake robot model consists of n cylindrical links that are connected by $n-1$ cardan joints, each having 2 DOFs. The distance L_i between two adjacent cardan joints equals the length of link i, and the radius of each link is L_{SC_i}. Each link is modeled as a cylinder of length $2L_{GS_i}$ with two spheres of radius L_{SC_i} attached to the ends the link. Link i with parts of its two adjacent links are illustrated in Fig. 2.

We denote an earth-fixed coordinate frame $I = (O, \boldsymbol{e}_x^I, \boldsymbol{e}_y^I, \boldsymbol{e}_z^I)$ (see Fig. 2) as an approximation to an inertial frame where its center O is fixed to the ground surface and the $\boldsymbol{e}_z^I$-axis is pointing in the opposite direction of the acceleration of gravity vector $\boldsymbol{g} = [\,0 \quad 0 \quad -g\,]^{\mathrm{T}}$. We denote a body-fixed frame $B_i = (G_i, \boldsymbol{e}_x^I, \boldsymbol{e}_y^I, \boldsymbol{e}_z^I)$, where G_i is the center of gravity of link i (which coincides with the geometric center of the link-cylinder) and $\boldsymbol{e}_z^I$ points along the center line of link i toward link $i+1$. A general notation used throughout this paper is that a vector from the origin of frame I to a point A is given by $\boldsymbol{r}_A$ and a vector from point A to point B is written as $\boldsymbol{r}_{AB}$. Let a vector $\boldsymbol{r}$ described in frame I be written as ${}_I\boldsymbol{r}$.

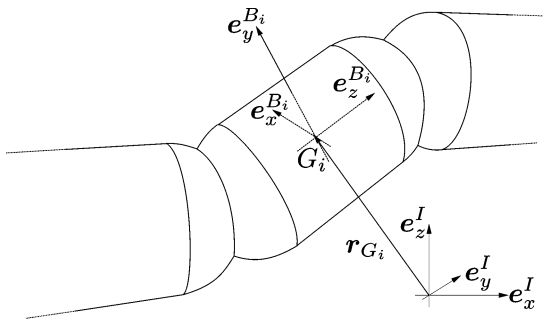

Fig. 2. Reference frames.

The position and orientation of link i are described by the *nonminimal absolute* coordinates [25]

$$\boldsymbol{q}_i = \begin{bmatrix} {}_I\boldsymbol{r}_{G_i} \\ \boldsymbol{p}_i \end{bmatrix} \in \mathbb{R}^7 \tag{4}$$

where ${}_I\boldsymbol{r}_{G_i} = [x_i \;\; y_i \;\; z_i]^{\mathrm{T}} \in \mathbb{R}^3$ is the position of the center of gravity of link i relative to frame i and the vector $\boldsymbol{p}_i = [e_{i_0} \;\; \boldsymbol{e}_i^{\mathrm{T}}]^{\mathrm{T}}$, where $\boldsymbol{e}_i^{\mathrm{T}} = [e_{i_1} \;\; e_{i_2} \;\; e_{i_3}]$, contains the four Euler parameters used to describe the rotation. The Euler parameters form a unit quaternion vector with the constraint $\boldsymbol{p}_i^{\mathrm{T}} \boldsymbol{p}_i = 1$. The coordinates are *nonminimal* because each link is described with six coordinates, and *absolute* because the position and orientation of link i is given directly relative to frame I. The velocity of link i is given by

$$\boldsymbol{u}_i = \begin{bmatrix} {}_I\boldsymbol{v}_{G_i} \\ {}_{B_i}\boldsymbol{\omega}_{IB_i} \end{bmatrix} \in \mathbb{R}^6 \tag{5}$$

where ${}_I\boldsymbol{v}_{G_i}$ is the translational velocity of the center of gravity of link i that is ${}_I\boldsymbol{v}_{G_i} = {}_I\dot{\boldsymbol{r}}_{G_i}$ when it exists (i.e., for impact-free motion). Moreover, ${}_{B_i}\boldsymbol{\omega}_{IB_i}$ is the angular velocity of frame B_i relative to frame I, given in frame B_i. The transformation ${}_I\boldsymbol{r} = \mathbf{R}^I_{B_i\ B_i}\boldsymbol{r}$ can be performed with the rotation matrix $\mathbf{R}^I_{B_i} = \mathbf{H}_i \bar{\mathbf{H}}_i^{\mathrm{T}}$, where

$$\mathbf{H}_i = [-\boldsymbol{e}_i \quad \tilde{\boldsymbol{e}}_i + e_{i_0}\mathbf{I}\,], \qquad \bar{\mathbf{H}}_i = [-\boldsymbol{e}_i \quad -\tilde{\boldsymbol{e}}_i + e_{i_0}\mathbf{I}\,] \tag{6}$$

and the superscript $\tilde{}$ denotes the skew-symmetric form of a vector throughout this paper, i.e.,

$$\tilde{\boldsymbol{e}} = \begin{bmatrix} 0 & -e_{i_3} & e_{i_2} \\ e_{i_3} & 0 & -e_{i_1} \\ -e_{i_2} & e_{i_1} & 0 \end{bmatrix}. \tag{7}$$

The time derivative of the rotation matrix is found from [26] as

$$\dot{\mathbf{R}}^I_{B_i} = \mathbf{R}^I_{B_i\ B_i}\tilde{\boldsymbol{\omega}}_{IB_i} = {}_I\tilde{\boldsymbol{\omega}}_{IB_i}\,\mathbf{R}^I_{B_i}. \tag{8}$$

The coordinates (positions and orientation) and velocities of all links are gathered in the vectors $\boldsymbol{q} = [\,\boldsymbol{q}_1^{\mathrm{T}} \quad \cdots \quad \boldsymbol{q}_n^{\mathrm{T}}]^{\mathrm{T}}$ and $\boldsymbol{u} = [\,\boldsymbol{u}_1^{\mathrm{T}} \quad \cdots \quad \boldsymbol{u}_n^{\mathrm{T}}\,]^{\mathrm{T}}$.

B. Gap Functions for Unilateral Constraints

Gap functions for the unilateral constraints (i.e., the ground surface) give the minimal distance between the floor and the front and rear part of each link. The contact surfaces between a

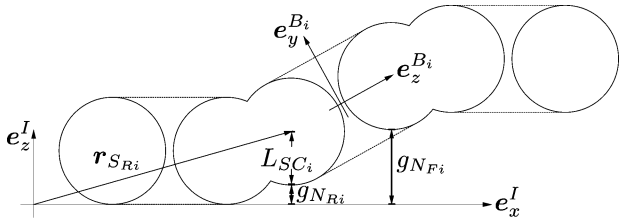

Fig. 3. Surfaces (solid-drawn circles) on snake robot that constitute the contact between the robot and the ground.

link and the ground are modeled as two spheres at the ends of the link, as illustrated for a three-link robot in Fig. 3.

We denote the distance between the center of the two spheres that belong to link i by $2L_{GS_i}$ and the radius of the spheres by L_{SC_i}. The position of the center of the front and rear spheres are denoted by $\boldsymbol{r}_{S_{Fi}}$ and $\boldsymbol{r}_{S_{Ri}}$, respectively. The shortest distance between the ground and the points on the front and rear spheres closest to the ground are denoted by $g_{N_{Fi}}$ and $g_{N_{Ri}}$, respectively. The distances are found from

$$g_{N_{Fi}} = (\boldsymbol{r}_{S_{Fi}})^{\mathrm{T}} \boldsymbol{e}_z^I - L_{SC_i}, \;\; g_{N_{Ri}} = (\boldsymbol{r}_{S_{Ri}})^{\mathrm{T}} \boldsymbol{e}_z^I - L_{SC_i} \quad (9)$$

where $\boldsymbol{r}_{S_{Fi}} = \boldsymbol{r}_{G_i} + L_{GS_i} \boldsymbol{e}_z^{B_i}$, $\boldsymbol{r}_{S_{Ri}} = \boldsymbol{r}_{G_i} - L_{GS_i} \boldsymbol{e}_z^{B_i}$.

The gap functions are gathered in the vector

$$\boldsymbol{g}_N = [\, g_{N_{F1}} \quad \cdots \quad g_{N_{Fn}} \quad g_{N_{R1}} \quad \cdots \quad g_{N_{Rn}} \,]^{\mathrm{T}}. \quad (10)$$

C. Gap Functions for Bilateral Constraints

Each 2 DOF cardan joint introduces four bilateral constraints, which will be described by gap functions.

To find the translational "gap" in the joints, we need to relate the position of the joint between link i and $i+1$ to both links. Let the position of the joint between link i and $i+1$ be written as ${}_I\boldsymbol{r}_{J_{Fi}} = {}_I\boldsymbol{r}_{G_i} + (1/2) L_i \, {}_I\boldsymbol{e}_z^{B_i}$, ${}_I\boldsymbol{r}_{J_{Ri+1}} = {}_I\boldsymbol{r}_{G_{i+1}} - (1/2) L_i \, {}_I\boldsymbol{e}_z^{B_{i+1}}$. The gap functions can now be found from

$$g_{J_{i\chi}} = \left({}_I\boldsymbol{r}_{J_{Fi}} - {}_I\boldsymbol{r}_{J_{Ri+1}} \right)^{\mathrm{T}} {}_I\boldsymbol{e}_\chi^I \quad (11)$$

for $i = 1, \ldots, n-1$, and $\chi = x, y, z$. Hence,

$$g_{J_{i\chi}} = \left({}_I\boldsymbol{r}_{G_i} - {}_I\boldsymbol{r}_{G_{i+1}} \right)^{\mathrm{T}} {}_I\boldsymbol{e}_\chi^I + \frac{1}{2} \left(L_i \mathbf{R}_{B_i \; B_i} \boldsymbol{e}_z^{B_i} + L_{i+1} \mathbf{R}_{B_{i+1} \; B_{i+1}} \boldsymbol{e}_z^{B_{i+1}} \right)^{\mathrm{T}} {}_I\boldsymbol{e}_\chi^I \quad (12)$$

for $i = 1, \ldots, n-1$.

The next gap function provides a "gap" in rotation around the axis that a cardan joint is not able to rotate around. Let $\boldsymbol{e}_y^{B_i}$ and $\boldsymbol{e}_x^{B_{i+1}}$ be the axes of rotation for the cardan joint between link i and link $i+1$, then $(\boldsymbol{e}_y^{B_i})^{\mathrm{T}} \boldsymbol{e}_x^{B_{i+1}} = 0$. Hence, a measure for the rotational "gap" can be defined from the previous equality as the gap function

$$g_{J_{i\phi}} = \left(\mathbf{R}^I_{B_i \; B_i} \boldsymbol{e}_y^{B_i} \right)^{\mathrm{T}} \left(\mathbf{R}^I_{B_{i+1} \; B_{i+1}} \boldsymbol{e}_x^{B_{i+1}} \right). \quad (13)$$

IV. Contact Constraints on Velocity Level

In this section, we calculate relative velocities between the snake robot and the ground from the gap functions. The relative velocities are needed to set up the set-valued contact forces for the closed contacts [27].

A. Unilateral Contact: Ground Contact

Contact between the snake robot and the ground involves (vertical) normal forces, which guarantee the unilaterality of the contact, and (horizontal) tangential contact forces, which are due to friction and are dependent on the normal contact forces and the relative sliding velocities.

1) Relative Velocities Along $\boldsymbol{e}_z^I$: The relative velocities between the front and rear part of link i and the ground along the $\boldsymbol{e}_z^I$-axis are defined as $\gamma_{N_{Fi}} := \dot{g}_{N_{Fi}}$ and $\gamma_{N_{Ri}} := \dot{g}_{N_{Ri}}$ (when they exist), respectively, and they are used later to find the normal contact forces. Before we proceed, note that $\gamma_{N_{Fi}}$ (or $\gamma_{N_{Ri}}$) should not be found directly by taking the time derivative of the expression for $g_{N_{Fi}}$ (or $g_{N_{Fi}}$) in (9). This is the case since the expressions (9) have already been simplified due to the fact that expressions have been inserted for the various body-fixed vectors that constitute the gap functions. Instead, for the relative velocities, we must consider the velocity of a *body-fixed* point P_{Fi} that, at time instant t, coincides with a point C_{Fi} on the front sphere closest to the ground (the same principle applies for the rear part of the link). Note that the position vectors for P_{F_i} and C_{F_i} will be the same instantaneously. However, the *differentials* will be different. This is shown in the following. Let C_{Fi} be a point on the front sphere that moves on the sphere such that the point is always closest to the ground surface. Then the position of this point is

$$\boldsymbol{r}_{C_{Fi}} = \boldsymbol{r}_{G_i} + \boldsymbol{r}_{G_i S_{Fi}} + \boldsymbol{r}_{S_{Fi} C_{Fi}}. \quad (14)$$

Define the skew-symmetric matrix ${}_I\tilde{\boldsymbol{r}}_{G_i C_{Fi}} = {}_I\tilde{\boldsymbol{r}}_{G_i S_{Fi}} + {}_I\tilde{\boldsymbol{r}}_{S_{Fi} C_{Fi}}$. The velocity of the point C_{Fi} is obtained by differentiation of (14) as

$${}_I\boldsymbol{v}_{C_{Fi}} = \underbrace{{}_I\boldsymbol{v}_{G_i} - {}_I\tilde{\boldsymbol{r}}_{G_i C_{Fi}} \mathbf{R}^I_{B_i \; B_i} \boldsymbol{\omega}_{IB_i}}_{{}_I\boldsymbol{v}_{P_{Fi}}} + \mathbf{R}^I_{B_i \; B_i} \dot{\boldsymbol{r}}_{S_{Fi} C_{Fi}} \quad (15)$$

where we now can use

$$\boldsymbol{r}_{S_{Fi} C_{Fi}} = -L_{SC_i} \boldsymbol{e}_z^I \quad (16)$$

and we have employed (8) and ${}_{B_i}\dot{\boldsymbol{r}}_{G_i S_{Fi}} = 0$, together with the identities ${}_I\tilde{\boldsymbol{\omega}}_{IB_i} \, {}_I\boldsymbol{r}_{G_i S_{Fi}} = -{}_I\boldsymbol{\omega}_{IB_i} \, {}_I\tilde{\boldsymbol{r}}_{G_i S_{Fi}}$ and ${}_I\tilde{\boldsymbol{\omega}}_{IB_i} \, {}_I\boldsymbol{r}_{S_{Fi} C_{Fi}} = -{}_I\boldsymbol{\omega}_{IB_i} \, {}_I\tilde{\boldsymbol{r}}_{S_{Fi} C_{Fi}}$. We see from (15) an expression for the velocity ${}_I\boldsymbol{v}_{P_{Fi}}$ of the body-fixed point P_{Fi} that, at time instant t, coincides with the point C_{Fi}. This velocity will be employed to find both the relative velocities along $\boldsymbol{e}_z^I$ and the tangential relative velocities. The equivalent velocity ${}_I\boldsymbol{v}_{P_{Ri}}$ on the rear part of the sphere is found similarly to ${}_I\boldsymbol{v}_{P_{Fi}}$ in (15) by replacing Fi by Ri in (15) and (16).

Now, the relative velocities along $\boldsymbol{e}_z^I$ for the front and rear part of link i can be found as

$$\gamma_{N_{Qi}} = ({}_I\boldsymbol{e}_z^I)^{\mathrm{T}} \, {}_I\boldsymbol{v}_{P_{Qi}} \Longrightarrow \gamma_{N_{Qi}} = (\boldsymbol{w}_{N_{Qi}})^{\mathrm{T}} \boldsymbol{u}_i \quad (17)$$

where

$$\boldsymbol{w}_{N_{Qi}} = [\,({}_I\boldsymbol{e}_z^I)^{\mathrm{T}} \quad -({}_I\boldsymbol{e}_z^I)^{\mathbf{T}}\,{}_I\tilde{\boldsymbol{r}}_{G_iC_{Qi}}\mathbf{R}_{B_i}^I\,]^{\mathrm{T}} \tag{18}$$

for $Q = F, R$ with $\boldsymbol{r}_{G_iS_{Fi}} = L_{GS_i}\,\boldsymbol{e}_z^{B_i}$ and $\boldsymbol{r}_{G_iS_{Ri}} = -L_{GS_i}\,\boldsymbol{e}_z^{B_i}$. The motivation to use the form (17) is that $\boldsymbol{w}_{N_{Qi}}$ gives the generalized direction of the contact force between the ground and the front and rear part of link i.

A vector gathering all $\gamma_{N_{Fi}}$ and $\gamma_{N_{Ri}}$ is

$$\gamma_N = \mathbf{W}_N^{\mathrm{T}}\boldsymbol{u} \tag{19}$$

where $[\gamma_N = [\,\gamma_{N_{F1}} \;\cdots\; \gamma_{N_{Fn}} \;\; \gamma_{N_{R1}} \;\cdots\; \gamma_{N_{Rn}}\,]^{\mathrm{T}}$, $\mathbf{W}_N = [\,\mathbf{W}_{N_F} \;\; \mathbf{W}_{N_R}\,] \in \mathbb{R}^{6n\times 2n}$, and

$$\mathbf{W}_{N_Q} = \begin{bmatrix} \boldsymbol{w}_{N_{Q1}} & \mathbf{0}_{6\times1} & \cdots & \mathbf{0}_{6\times1} \\ \mathbf{0}_{6\times1} & \ddots & & \vdots \\ \vdots & & \ddots & \mathbf{0}_{6\times1} \\ \mathbf{0}_{6\times1} & \cdots & \mathbf{0}_{6\times1} & \boldsymbol{w}_{N_{Qn}} \end{bmatrix} \tag{20}$$

for $Q = F, R$.

2) Tangential Relative Velocities: Friction forces between a link and the ground depend on the relative velocities in the $(\boldsymbol{e}_x^I, \boldsymbol{e}_y^I)$-plane between the snake robot links and the ground. These velocities are termed tangential relative velocities. First, the relative velocities between the front part of link i and the ground along the $\boldsymbol{e}_x^I$- and $\boldsymbol{e}_y^I$-axis, $\gamma'_{T_{Fix}}$ and $\gamma'_{T_{Fiy}}$, will be deducted. Subsequently, the relative velocities for the front part of link i along the projection of the longitudinal axis of the link onto the $(\boldsymbol{e}_x^I, \boldsymbol{e}_y^I)$-plane $\gamma_{T_{Fix}}$ and transversal to the link $\gamma_{T_{Fiy}}$, will be deducted from $\gamma'_{T_{Fix}}$ and $\gamma'_{T_{Fiy}}$, respectively. The same type of notation applies for the rear part of link i: $\gamma'_{T_{Rix}}$, $\gamma'_{T_{Riy}}$, $\gamma_{T_{Rix}}$, and $\gamma_{T_{Riy}}$. The tangential relative velocities are found much in the same way as for $\gamma_{N_{Fi}}$ and $\gamma_{N_{Ri}}$. Consequently, we find the velocities of the points P_{Fi} and P_{Ri} along the $\boldsymbol{e}_x^I$- and $\boldsymbol{e}_y^I$-axis. Hence, by looking at (17), we see that the tangential relative velocities of the contact points on the front part of the link can be found as

$$\gamma'_{T_{Fi\zeta}} = ({}_I\boldsymbol{e}_\zeta^I)^{\mathbf{T}}\,{}_I\boldsymbol{v}_{P_{Fi}} \Longrightarrow \gamma'_{T_{Fi\zeta}} = (\boldsymbol{w}'_{T_{Fi\zeta}})^{\mathrm{T}}\boldsymbol{u}_i \tag{21}$$

for $\zeta = x, y$, where

$$\boldsymbol{w}'_{T_{Fi\zeta}} = [\,({}_I\boldsymbol{e}_\zeta^I)^{\mathrm{T}} \quad -({}_I\boldsymbol{e}_\zeta^I)^{\mathrm{T}}\,{}_I\tilde{\boldsymbol{r}}_{G_iC_{Fi}}\mathbf{R}_{B_i}^I\,]^{\mathrm{T}}. \tag{22}$$

The relative velocities between the rear part of the link and the ground are found by exchanging ${}_I\boldsymbol{v}_{P_{Fi}}$ with ${}_I\boldsymbol{v}_{P_{Ri}}$ in (21)

$$\gamma'_{T_{Ri\zeta}} = ({}_I\boldsymbol{e}_\zeta^I)^{\mathrm{T}}\,{}_I\boldsymbol{v}_{P_{Ri}} \Longrightarrow \gamma'_{T_{Ri\zeta}} = (\boldsymbol{w}'_{T_{Ri\zeta}})^{\mathrm{T}}\boldsymbol{u}_i \tag{23}$$

for $\zeta = x, y$, where

$$\boldsymbol{w}'_{T_{Ri\zeta}} = [\,({}_I\boldsymbol{e}_\zeta^I)^{\mathrm{T}} \quad -({}_I\boldsymbol{e}_\zeta^I)^{\mathrm{T}}\,{}_I\tilde{\boldsymbol{r}}_{G_iC_{Fi}}\mathbf{R}_{B_i}^I\,]^{\mathrm{T}}. \tag{24}$$

The tangential relative velocities for the front and rear part of the link i are combined in vectors

$$\gamma'_{T_{Qi}} = \mathbf{W}'^{\mathrm{T}}_{T_{Qi}}\boldsymbol{u}_i \tag{25}$$

for $Q = F,\ R$, where $\gamma'_{T_{Qi}} = [\,\gamma'_{T_{Qix}} \;\; \gamma'_{T_{Qiy}}\,]^{\mathrm{T}}$ and

$$\mathbf{W}'_{T_{Qi}} = [\,\boldsymbol{w}'_{T_{Qix}} \;\; \boldsymbol{w}'_{T_{Qiy}}\,] \in \mathbb{R}^{6\times2}. \tag{26}$$

Until now, the relative velocities have been given in the directions along the $\boldsymbol{e}_x^I$- and $\boldsymbol{e}_y^I$-axes. In order to calculate the friction forces longitudinal and transversal to a link, we need to know the corresponding relative velocities in these directions in the $(\boldsymbol{e}_x^I, \boldsymbol{e}_y^I)$-plane. To calculate these velocities, we introduce for each link a frame Π_i with axes $(\boldsymbol{e}_x^{\Pi_i}, \boldsymbol{e}_y^{\Pi_i}, \boldsymbol{e}_z^{\Pi_i})$, where ${}_I\boldsymbol{e}_z^{\Pi_i} = {}_I\boldsymbol{e}_z^I$, and

$${}_I\boldsymbol{e}_x^{\Pi_i} = \frac{\mathbf{A}_{xy}\,{}_I\mathbf{e}_z^{B_i}}{\|\mathbf{A}_{xy}\,{}_I\mathbf{e}_z^{B_i}\|}, \quad {}_I\mathbf{e}_y^{\Pi_i} = \frac{{}_I\mathbf{e}_z^I \times {}_I\mathbf{e}_x^{\Pi_i}}{\|\,{}_I\mathbf{e}_z^I \times {}_I\mathbf{e}_x^{\Pi_i}\|} \tag{27}$$

where $\mathbf{A}_{xy} = \mathrm{diag}([1,\ 1,\ 0])$. Hence, it holds that

$$\mathbf{R}_{\Pi_i}^I = [\,{}_I\boldsymbol{e}_x^{\Pi_i} \quad {}_I\boldsymbol{e}_y^{\Pi_i} \quad {}_I\boldsymbol{e}_z^{\Pi_i}\,]. \tag{28}$$

Notice that ${}_I\boldsymbol{e}_x^{\Pi_i} = {}_I\boldsymbol{e}_z^{B_i}$ and ${}_I\boldsymbol{e}_y^{\Pi_i} = {}_I\boldsymbol{e}_x^{B_i}$ when link i is lying flat on the ground with ${}_I\boldsymbol{e}_y^{B_i} = {}_I\boldsymbol{e}_z^I$. Since only the motion in the $(\boldsymbol{e}_x^I, \boldsymbol{e}_y^I)$ -plane is of interest, we define

$$\bar{\mathbf{R}}_{\Pi_i}^I = \mathbf{D}^{\mathrm{T}}\mathbf{R}_{\Pi_i}^I\mathbf{D}, \qquad \mathbf{D} = \begin{bmatrix} 1 & 0 & 0 \\ 0 & 1 & 0 \end{bmatrix}^{\mathrm{T}}. \tag{29}$$

Since we now have that $\boldsymbol{\gamma}'_{T_{Qi}} = \bar{\mathbf{R}}_{\Pi_i}^I\boldsymbol{\gamma}_{T_{Qi}}$, $Q = F,\ R$, the relative velocity between the floor and the front part of link i, with respect to frame Π_i, can be found from (25) as

$$\boldsymbol{\gamma}_{T_{Qi}} = \mathbf{W}_{T_{Qi}}^{\mathrm{T}}\boldsymbol{u}_i \tag{30}$$

where $\boldsymbol{\gamma}_{T_{Qi}} = [\,\boldsymbol{\gamma}_{T_{Qix}} \quad \boldsymbol{\gamma}_{T_{Qiy}}\,]^{\mathrm{T}}$, $\mathbf{W}_{T_{Qi}} = \mathbf{W}'_{T_{Qi}}\bar{\mathbf{R}}_{\Pi_i}^I$, for $Q = F, R$.

A vector that gathers all $\boldsymbol{\gamma}_{T_{Fi}}$ and $\boldsymbol{\gamma}_{T_{Ri}}$ is found from

$$\boldsymbol{\gamma}_T = \mathbf{W}_T^{\mathrm{T}}\boldsymbol{u} \tag{31}$$

where

$$\boldsymbol{\gamma}_T = [\,\boldsymbol{\gamma}_{T_{F1}}^{\mathrm{T}} \;\cdots\; \boldsymbol{\gamma}_{T_{Fn}}^{\mathrm{T}} \;\; \boldsymbol{\gamma}_{T_{R1}}^{\mathrm{T}} \;\cdots\; \boldsymbol{\gamma}_{T_{Rn}}^{\mathrm{T}}\,]^{\mathrm{T}} \tag{32}$$

$\mathbf{W}_T = [\,\mathbf{W}_{T_F} \quad \mathbf{W}_{T_R}\,] \in \mathbb{R}^{6n\times4n}$, and $\mathbf{W}_{T_F}$, $\mathbf{W}_{T_R}$ are found similarly to (20) by replacing the zero vectors with $\mathbf{0}_{6\times2}$ and replacing the vectors $\boldsymbol{w}_{N_{Fi}}$, $\boldsymbol{w}_{N_{Ri}}$ with the matrices $\mathbf{W}_{T_{Fi}}$, $\mathbf{W}_{T_{Ri}}$, respectively.

3) Relative Rolling Velocities: Up until now, we have only considered the translational relative motion of the snake robot links. However, we also need to consider rotational relative motion to add a damping effect on the rotational motion in the form of rotational friction. In order to do this, we introduce a relative rolling velocity as

$$\boldsymbol{\gamma}_{V_{Qi}} = \mathbf{D}^{\mathrm{T}}\left({}_I\boldsymbol{r}_{C_{Qi}S_{Qi}} \times {}_I\boldsymbol{\omega}_{IB_i}\right) \tag{33}$$

for $Q = F, \quad R$, where $\boldsymbol{\gamma}_{V_{Qi}} = [\,\gamma_{V_{Qix}} \quad \gamma_{V_{Qiy}}\,]^{\mathrm{T}}$ and ${}_I\boldsymbol{r}_{C_{Qi}S_{Qi}} = L_{SC_i}\,{}_I\boldsymbol{e}_z^I$ is the vector pointing (upwards) from the body-fixed point C_{Q_i} on the link end sphere momentarily closest to the ground, toward the center S_{Q_i} of the end sphere. By employing the identity

$${}_I\boldsymbol{r}_{C_{Qi}S_{Qi}} \times {}_I\boldsymbol{\omega}_{IB_i} = {}_I\tilde{\boldsymbol{r}}_{C_{Qi}S_{Qi}}\mathbf{R}_{B_i}^I\,{}_{B_i}\boldsymbol{\omega}_{IB_i} \tag{34}$$

we find that the relative rolling velocity can be written as

$$\gamma_{V_{Qi}} = \mathbf{W}_{V_{Qi}}^{\mathrm{T}}\,\boldsymbol{u}_i \tag{35}$$

where

$$\mathbf{W}_{V_{Q\,i}}^{\mathrm{T}} = [\,\mathbf{O}_{2\times 3} \quad \mathbf{D}^{\mathrm{T}}{}_{I}\tilde{\boldsymbol{r}}_{C_{Q\,i}S_{Q\,i}}\mathbf{R}_{B_i}^{I}\,] \tag{36}$$

for $Q = F, R$.

We gather all the relative rolling velocities as

$$\boldsymbol{\gamma}_V = \mathbf{W}_V \boldsymbol{u} \tag{37}$$

where $\boldsymbol{\gamma}_V = [\,\boldsymbol{\gamma}_{V_{F1}}^{\mathrm{T}} \cdots \boldsymbol{\gamma}_{V_{Fn}}^{\mathrm{T}} \;\; \boldsymbol{\gamma}_{V_{R1}}^{\mathrm{T}} \cdots \boldsymbol{\gamma}_{V_{Rn}}^{\mathrm{T}}\,]^{\mathrm{T}}$, $\mathbf{W}_V = [\,\mathbf{W}_{V_F} \;\; \mathbf{W}_{V_R}\,] \in \mathbb{R}^{6n\times 4n}$, and $\mathbf{W}_{V_F}$, $\mathbf{W}_{V_R}$ are found similarly to (20) by replacing the zero vectors with $\mathbf{0}_{6\times 2}$ and replacing the vectors $\boldsymbol{w}_{N_{F\,i}}$, $\boldsymbol{w}_{N_{R\,i}}$ with the matrices $\mathbf{W}_{V_{F\,i}}$, $\mathbf{W}_{V_{R\,i}}$, respectively.

B. Bilateral Constraints: Joints

Bilateral constraints introduced by the cardan joint between two adjacent links prohibit relative motion between the links in 4 DOFs. The relative velocities between the links along these DOFs need to be found in order to calculate the bilateral constraint forces in the joints. These relative velocities are found from the gap functions (12) and (13).

Relative velocities for the translational gap between link i and link $i+1$ are defined as $\gamma_{J_{i\chi}} := \dot{g}_{J_{i\chi}}$, for $i = 1, \ldots, n-1$, where $\chi = x, y, z$. By employing (12), we find that

$$\gamma_{J_{i\chi}} = \boldsymbol{w}_{J_{i\chi}}^{\mathrm{T}} \begin{bmatrix} \boldsymbol{u}_i \\ \boldsymbol{u}_{i+1} \end{bmatrix} \tag{38}$$

where

$$\boldsymbol{w}_{J_{i\chi}} = \begin{bmatrix} ({}_I\boldsymbol{e}_\chi^I) \\ -\left(({}_I\boldsymbol{e}_\chi^I)^{\mathrm{T}}\frac{L_i}{2}\mathbf{R}_{B_i\;B_i}^{I}\tilde{\boldsymbol{e}}_z^{B_i}\right)^{\mathrm{T}} \\ -({}_I\boldsymbol{e}_\chi^I) \\ -\left(({}_I\boldsymbol{e}_\chi^I)^{\mathrm{T}}(L_{i+1}/2)\mathbf{R}_{B_{i+1}\;B_{i+1}}^{I}\tilde{\boldsymbol{e}}_z^{B_{i+1}}\right)^{\mathrm{T}} \end{bmatrix}. \tag{39}$$

A relative velocity for the rotational gap is defined as $\gamma_{J_{i\phi}} := \dot{g}_{J_{i\phi}}$, for $i = 1, \ldots, n-1$. Hence,

$$\gamma_{J_{i\phi}} = \boldsymbol{w}_{J_{i\phi}}^{\mathrm{T}} \begin{bmatrix} \boldsymbol{u}_i \\ \boldsymbol{u}_{i+1} \end{bmatrix} \tag{40}$$

where

$$\boldsymbol{w}_{J_{i\phi}} = \begin{bmatrix} \mathbf{0}_{3\times 1} \\ -\left(\mathbf{R}_{B_i\;B_i}^{I}\tilde{\boldsymbol{e}}_y^{B_i}\right)^{\mathrm{T}}\left(\mathbf{R}_{B_{i+1}\;B_{i+1}}^{I}\boldsymbol{e}_x^{B_{i+1}}\right) \\ \mathbf{0}_{3\times 1} \\ -\left(\mathbf{R}_{B_{i+1}\;B_{i+1}}^{I}\tilde{\boldsymbol{e}}_x^{B_{i+1}}\right)^{\mathrm{T}}\left(\mathbf{R}_{B_i\;B_i}^{I}\boldsymbol{e}_y^{B_i}\right) \end{bmatrix}. \tag{41}$$

Let $\gamma_{J_i} = [\,\gamma_{J_{ix}} \;\; \gamma_{J_{iy}} \;\; \gamma_{J_{iz}} \;\; \gamma_{J_{i\phi}}\,]^{\mathrm{T}}$, then we can gather all the relative velocities concerned with the bilateral constraints in one vector

$$\boldsymbol{\gamma}_J = \mathbf{W}_J^{\mathrm{T}}\boldsymbol{u} \tag{42}$$

where $\boldsymbol{\gamma}_J = [\,\boldsymbol{\gamma}_{J_1}^{\mathrm{T}} \cdots \boldsymbol{\gamma}_{J_{n-1}}^{\mathrm{T}}\,]^{\mathrm{T}}$,

$$\mathbf{W}_J = \begin{bmatrix} \mathbf{W}_{J1}^{\mathrm{T}} & \mathbf{0}_{4\times 6} & \cdots & \mathbf{0}_{4\times 6} \\ \mathbf{0}_{4\times 6} & \mathbf{W}_{J2}^{\mathrm{T}} & & \vdots \\ \vdots & & \ddots & \mathbf{0}_{4\times 6} \\ \mathbf{0}_{4\times 6} & \cdots & \mathbf{0}_{4\times 6} & \mathbf{W}_{Jn-1}^{\mathrm{T}} \end{bmatrix}^{\mathrm{T}} \in \mathbb{R}^{6n\times 4(n-1)} \tag{43}$$

and $\mathbf{W}_{Ji} = [\,\boldsymbol{w}_{J_{ix}} \;\; \boldsymbol{w}_{J_{iy}} \;\; \boldsymbol{w}_{J_{iz}} \;\; \boldsymbol{w}_{J_{i\phi}}\,] \in \mathbb{R}^{12\times 4}$, for $i = 1, \ldots, n-1$.

V. Nonsmooth Dynamics

The starting point for describing the dynamics of the snake robot is the *equality of measures* as introduced in [23]. The equality of measures includes equations of motion for impact-free motion as well as impact equations. The impact equations give rise to impulsive behavior [24]. In this section, we employ the results from Sections III and Section IV in order to find the equality of measures for the snake robot.

A. Equality of Measures

An equality of measures describes the dynamics of the snake robot within the context of nonsmooth dynamics. Velocity jumps, usually associated with impacts, are modeled to occur instantaneously. Hence, the time derivative of a velocity does not always exist. By considering the generalized velocity to be a function $t \mapsto \boldsymbol{u}(t)$ of locally bounded variation on a time interval $I = [\,t_A, t_E\,]$ [23], the function $\boldsymbol{u}(t)$ admits a right $\boldsymbol{u}^+$ and left $\boldsymbol{u}^-$ limit for all $t \in I$, and its time derivative $\dot{\boldsymbol{u}}$ exists for almost all $t \in I$. To be able to obtain $\boldsymbol{u}$ from integration, we need to use the differential measure $\mathrm{d}\boldsymbol{u}$, where it is assumed that the measure can be decomposed into

$$\mathrm{d}\boldsymbol{u} = \dot{\boldsymbol{u}}\,\mathrm{d}t + \left(\boldsymbol{u}^+ - \boldsymbol{u}^-\right)\mathrm{d}\eta \tag{44}$$

where $\mathrm{d}t$ denotes the Lebesgue measure and $\mathrm{d}\eta$ denotes the atomic measure where $\int_{\{t_1\}}\mathrm{d}\eta = 1$. The total increment of $\boldsymbol{u}$ over a compact subinterval $[t_1, t_2]$ of I is found as

$$\int_{[t_1,t_2]}\mathrm{d}\boldsymbol{u} = \boldsymbol{u}^+(t_2) - \boldsymbol{u}^-(t_1) \tag{45}$$

and is due to a continuous change (i.e., impact-free motion) stemming from $\dot{\boldsymbol{u}}$ as well as possible discontinuities in $\boldsymbol{u}$ due to impacts within the time interval $[t_1, t_2]$. Equation (45) is also valid when the time interval reduces to a singleton $\{t_1\}$, and if a velocity jump occurs for $t = t_1$, then (45) gives a nonzero result.

From the earlier notation, the Newton–Euler equations as an equality of measures can be written in a general form as

$$\mathbf{M}(\boldsymbol{q}, t)\,\mathrm{d}\boldsymbol{u} - \boldsymbol{h}(\boldsymbol{q}, \boldsymbol{u}, t)\,\mathrm{d}t - \mathrm{d}\boldsymbol{R} = \boldsymbol{\tau}_C\,\mathrm{d}t \tag{46}$$

where the mass matrix $\mathbf{M}(\boldsymbol{q}, t)$, the vector of smooth forces $\boldsymbol{h}(\boldsymbol{q}, \boldsymbol{u}, t)$, the force measure of possibly atomic impact impulsions $\mathrm{d}\boldsymbol{R}$, and the vector of applied torques $\boldsymbol{\tau}_C$ will be described in the following.

For our choice of coordinates, the mass matrix is *diagonal* and constant

$$\mathbf{M}(\boldsymbol{q},t)=\mathbf{M}=\begin{bmatrix}\mathbf{M}_1 & & \mathbf{0}\\ & \ddots & \\ \mathbf{0} & & \mathbf{M}_n\end{bmatrix}\in\mathbb{R}^{6n\times 6n} \tag{47}$$

where

$$\mathbf{M}_i=\begin{bmatrix}m_i\mathbf{I}_{3\times 3} & \mathbf{0}_{3\times 3}\\ \mathbf{0}_{3\times 3} & {}_{B_i}\boldsymbol{\Theta}_{G_i}\end{bmatrix} \tag{48}$$

with ${}_{B_i}\Theta_{G_i}=\mathrm{diag}([\Theta_{1i}\quad\Theta_{1i}\quad\Theta_{3i}])$, m_i is the mass of link i, and Θ_{1i} and Θ_{3i} are its moments of inertia. The smooth forces, here consisting of gravity and gyroscopic accelerations, are described by $\boldsymbol{h}(\boldsymbol{q},\boldsymbol{u},t)=\boldsymbol{h}(\boldsymbol{u})=[\boldsymbol{h}_1^{\mathrm{T}}(\boldsymbol{u}_1)\quad\cdots\quad\boldsymbol{h}_n^{\mathrm{T}}(\boldsymbol{u}_n)]^{\mathrm{T}}\in\mathbb{R}^{6n}$, where $\boldsymbol{h}_i(\boldsymbol{u}_i)=[0\quad 0\quad -m_ig\quad -({}_{B_i}\tilde{\boldsymbol{\omega}}_{IB_i}\,{}_{B_i}\Theta_{G_i}\,{}_{B_i}\boldsymbol{\omega}_{IB_i})^{\mathrm{T}}]^{\mathrm{T}}$.

The force measure $\mathrm{d}\boldsymbol{R}$ accounts for all the contact forces and impulses. The contact efforts that constitute $\mathrm{d}\boldsymbol{R}$ are found from the force laws given in Section V-B. Let $\mathcal{I}$ be the set of all active contacts with the ground

$$\mathcal{I}(t)=\{a\mid g_{N_a}(\boldsymbol{q}(t))=0\}\subseteq\{1,2,\ldots,2n\} \tag{49}$$

where g_{N_a} is the ath element of the vector $\boldsymbol{g}_N$ in (10). Now, the force measure is written as

$$\begin{aligned}\mathrm{d}\boldsymbol{R}=\mathbf{W}_J\,\mathrm{d}\boldsymbol{P}_J&+\sum_{a\in\mathcal{I}}(\mathbf{W}_N)_a\,\mathrm{d}P_{N_a}\\&+\sum_{a\in\mathcal{I}}\left((\mathbf{W}_T)_{2a-1}\,\mathrm{d}P_{T_{ax}}+(\mathbf{W}_T)_{2a}\,\mathrm{d}P_{T_{ay}}\right)\\&+\sum_{a\in\mathcal{I}}\left((\mathbf{W}_V)_{2a-1}\,\mathrm{d}P_{V_{ax}}+(\mathbf{W}_V)_{2a}\,\mathrm{d}P_{V_{ay}}\right)\end{aligned} \tag{50}$$

where $\mathrm{d}P_{N_a}$ is the normal contact impulse measure between the ground and a link, $\mathrm{d}P_{T_{ax}}$ and $\mathrm{d}P_{T_{ay}}$ are the tangential contact impulse measures (friction) between the floor and a link, longitudinal and transversal to the link (i.e., along the $\boldsymbol{e}_x^{\Pi_i}$- and $\boldsymbol{e}_y^{\Pi_i}$-axis), respectively, $\mathrm{d}P_{V_{ax}}$ and $\mathrm{d}P_{V_{ay}}$ are the rotational contact impulse measures (friction) between the floor and a link, along the $\boldsymbol{e}_x^I$-axis and $\boldsymbol{e}_y^I$-axis, respectively, $\mathrm{d}\boldsymbol{P}_J$ is the contact impulse measure due to the bilateral constraints in the joints (these constraints are always active), and the lower case subscripts on the $\mathbf{W}$ matrices indicate which column of the matrix is used. The position of the elements of the vectors $\mathrm{d}\boldsymbol{P}_N$, $\mathrm{d}\boldsymbol{P}_J$, $\mathrm{d}\boldsymbol{P}_T$, and $\mathrm{d}\boldsymbol{P}_V$ corresponds to the position of the elements in their respective vector of relative velocity $\boldsymbol{\gamma}_N$, $\boldsymbol{\gamma}_J$, $\boldsymbol{\gamma}_T$, and $\boldsymbol{\gamma}_V$. Hence, looking at, for example, the expression (32) for $\boldsymbol{\gamma}_T$, we see that, e.g., $\mathrm{d}\boldsymbol{P}_{T_{n+1}}=[\mathrm{d}P_{T_{(n+1)x}}\;\mathrm{d}P_{T_{(n+1)y}}]^{\mathrm{T}}$ corresponds to $\boldsymbol{\gamma}_{T_{R1}}$, and we know from this that $\mathrm{d}\boldsymbol{P}_{T_{n+1}}$ is the tangential contact impulse measure between the ground and the rear part of link 1.

The contact impulse measures can be decomposed in the same way as for $\mathrm{d}\boldsymbol{u}$. Let us take the normal contact impulse measure as an example. The measure can be written as

$$\mathrm{d}P_{N_a}=\lambda_{N_a}\,\mathrm{d}t+\Lambda_{N_a}\,\mathrm{d}\eta \tag{51}$$

where λ_{N_a} is the Lebesgue-measurable force and Λ_{N_a} is the purely atomic impact impulse. The same decomposition can also be performed for the other three impulse measures.

The control torques $\boldsymbol{\tau}_C$ are described in Section V-C.

B. Constitutive Laws for the Contact Forces

In this section, we will introduce set-valued force laws for normal contact and Coulomb friction. These laws will all be formulated on velocity level using the relative contact velocities γ given by (19) and (31). Subsequently, the set-valued force laws are formulated as equalities in Section V-B.4 using the so-called proximal point function in order to include the force laws in the numerical simulation [22].

1) Normal Contact Force: The normal contact between a link and the floor is described by the unilateral constraint

$$g_N\geq 0,\qquad \lambda_N\geq 0,\qquad g_N\lambda_N=0 \tag{52}$$

which is known as Signorini's law [22]. Here, λ_N is the normal contact force and g_N is the gap function. Subscripts Ri and Fi are temporarily removed for simplicity. This set-valued force law states that the contact is impenetrable, $g_N\geq 0$, the contact can only transmit pressure forces $\lambda_N\geq 0$, and the contact force λ_N does not produce work $g_N\lambda_N=0$. The force law can be expressed on different kinematic levels: displacement level (52), velocity level, and acceleration level. In the following, we express all force laws for closed contact on velocity level, while all forces vanish for open contacts. Then, by employing concepts of convex analysis, the relationship between the relative velocity and the Lebesgue-measurable normal contact force (not an impulse) may be written for a closed contact $g_N=0$ as an inclusion on velocity level

$$-\gamma_N\in N_{C_N}(\lambda_N) \tag{53}$$

where the convex set $C_N=\{\lambda_N\mid\lambda_N\geq 0\}=\mathbb{R}^+$ is the set of admissible contact forces, and N_{C_N} is the normal cone to C_N [22]. The inclusion (53) is equivalent to the condition

$$\gamma_N\geq 0,\qquad \lambda_N\geq 0,\qquad \gamma_N\lambda_N=0 \tag{54}$$

for a closed contact $g_N=0$. Before explaining the force law (53), let us first mention that this force law describes the impenetrability of sustained contact, i.e., $g_N=0$ and $\gamma_N=0$, as well as the detachment: $\gamma_N>0\Rightarrow\lambda_N=0$. However, (53) does not cover impacts (where we have impulses instead of forces). For impacts, we need a similar *impact law* described at the end of this section.

From the definition [22], [28] of a normal cone $N_C(\mathbf{x})$ to a convex set C at the point $\boldsymbol{x}\in\mathbb{R}^n$, we have that $N_C(\boldsymbol{x})=\{0\}$, for $\boldsymbol{x}\in\mathrm{int}\;C$, and $N_C(\boldsymbol{x})=\{\emptyset\}$, for $\boldsymbol{x}\notin C$. If $\boldsymbol{x}$ is on the *boundary* of C, then $N_C(\boldsymbol{x})$ is the set of all vectors $\boldsymbol{y}\in\mathbb{R}^n$ that are normal to $\boldsymbol{x}$. For example, for $C_N=\mathbb{R}^+$, we have $N_{C_N}(0)=\mathbb{R}^-$ and $N_{C_N}(2)=0$.

The force law (53) only covers finite-valued contact efforts during impulse-free motion, i.e., all velocities are absolutely continuous in time. When a collision occurs in a rigid-body setting, then the velocities will be locally discontinuous in order to prevent penetration. The velocity jump is accompanied by an

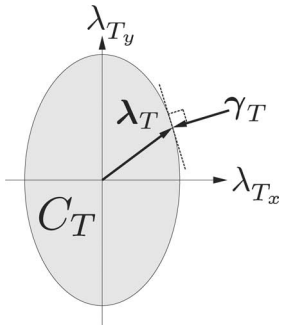

Fig. 4. Relationship between tangential relative velocity and friction force. The set C_T is in gray.

impact impulse Λ_N, for which we will set up an impact law. The relative velocity admits, similarly to the velocities $\boldsymbol{u}$, a right γ_N^+ and a left γ_N^- limit. The impact law for a completely inelastic impact at a closed contact can now be written as

$$-\gamma_N^+ \in N_{C_N}(\Lambda_N), \qquad C_N = \{\Lambda_N \mid \Lambda_N \geq 0\} = \mathbb{R}^+ \quad (55)$$

which is equivalent to the condition

$$\gamma_N^+ \geq 0, \qquad \Lambda_N \geq 0, \qquad \gamma_N^+ \Lambda_N = 0. \quad (56)$$

Notice that the force law (53) and impact law (55) is on the same form. We have earlier stated that there is no need for an explicit switch between equations when, e.g., an impact occurs. This becomes evident in Section VII with the introduction of the contact impulse (that includes both forces and possible impulses) for the discretization of the system dynamics.

The force law for normal contact given in this section can also be employed to describe normal contact with obstacles. This is described in [29].

2) Coulomb Friction Force: In this section, we describe the friction force between the snake robot and the ground when the snake robot slides along the ground surface as set-valued Coulomb friction. Similarly to the force law (53) for normal contact, we describe the constitutive description for friction using an inclusion on a normal cone. The friction force $\boldsymbol{\lambda}_T$, in the 2-D tangent plane to the contact point, is modeled with an anisotropic Coulomb friction law

$$-\boldsymbol{\gamma}_T \in N_{C_T}(\boldsymbol{\lambda}_T) \quad (57)$$

where $\boldsymbol{\gamma}_T$ is a relative sliding velocity, N_{C_T} is the normal cone to the set C_T, and the ellipse

$$C_T = \left\{ \boldsymbol{\lambda}_T \;\middle|\; \frac{\lambda_{T_x}^2}{\left(\mu_{T_x}\lambda_N\right)^2} + \frac{\lambda_{T_y}^2}{\left(\mu_{T_y}\lambda_N\right)^2} \leq 1 \right\} \quad (58)$$

is the set of admissible friction forces, where $\boldsymbol{\lambda}_T = [\lambda_{T_x} \quad \lambda_{T_y}]^{\mathrm{T}}$, and μ_{T_x}, $\mu_{T_y} > 0$ are directional friction coefficients along the $\boldsymbol{e}_x^{\Pi}$- and $\boldsymbol{e}_y^{\Pi}$-axis from (27), respectively. Fig. 4 depicts the set C_T (in gray), together with the relationship between the tangential relative velocities and the friction force when it is on the boundary of C_T.

The force law (57) distinguishes between two cases: if the friction force is in the interior of C_T or on its boundary. If $\boldsymbol{\lambda}_T \in \text{int}\, C_T$, then it holds that $N_{C_T}(\boldsymbol{\lambda}_T) = \mathbf{0}$ from which we conclude that $\boldsymbol{\gamma}_T = \mathbf{0}$. Obviously, this corresponds to the stick phase of the friction law. If the friction force is on the boundary of C_T, then the normal cone $N_{C_T}(\boldsymbol{\lambda}_T)$ consists of the outward normal ray on the ellipse C_T at the point $\boldsymbol{\lambda}_T$.

The advantage to formulate the friction law as the inclusion (57) now becomes apparent. First of all, note that (57) is a *spatial* friction law. Such a spatial friction law cannot properly be described by a set-valued sign function. Some authors [10], [12] model the spatial contact with two sign functions for the two components of the relative sliding velocity using two friction coefficients μ_{T_x} and μ_{T_y}. Others smoothen the (set-valued) sign function with a smoothening function, e.g., some arctangent function. This results in a very steep slope of the friction curve near zero relative velocity. Such an approach is very cumbersome for two reasons. First of all, stiction cannot properly be described: an object on a slope will with a smoothened friction law always slide. Second, the very steep slope of the friction curve causes the differential equations of motion to become numerically stiff. Summarizing, we see that (57) describes spatial Coulomb friction taking stiction properly into account.

While the force law (57) only describes the Coulomb friction during impulse-free motion, we also need a force law for impact impulses $\boldsymbol{\lambda}_T$. These are found from the exact same form as (57) by replacing $\boldsymbol{\gamma}_T$ with its right limit $\boldsymbol{\gamma}_T^+$ and inserting $\boldsymbol{\lambda}_T$ instead of $\boldsymbol{\lambda}_T$ both in (57) and in the convex set C_T in (58).

3) Rolling Friction: The snake robot modeled in this paper has cylindrical links which means that it may roll sideways. The spatial Coulomb friction described in the previous section arises from translational motion. In addition, there is also a force that resists the rolling motion of the snake robot. We model this force as a "rolling friction" $\boldsymbol{\lambda}_V \in \mathbb{R}^2$ (additional subscripts omitted for simplicity) in this paper by employing the same set-valued force law as for the tangential Coulomb friction force $\boldsymbol{\lambda}_T$ in Section V-B2. However, we consider the rolling friction to be isotropic, and therefore, we find the rolling friction as

$$-\boldsymbol{\gamma}_V \in N_{C_V}(\boldsymbol{\lambda}_V) \quad (59)$$

where

$$C_V = \{\boldsymbol{\lambda}_V \mid \|\boldsymbol{\lambda}_V\| \leq \mu_V \boldsymbol{\lambda}_N\} \quad (60)$$

and $\mu_V > 0$ is the friction coefficient.

The general form of the force law (59) is also valid for impact impulses $\boldsymbol{\Lambda}_V$ in the same way as for the tangential Coulomb friction described in Section V-B2. Subsequently, the impact impulse is found by exchanging $\boldsymbol{\gamma}_V$ with $\boldsymbol{\gamma}_V^+$ and $\boldsymbol{\lambda}_V$ with $\boldsymbol{\Lambda}_V$ in (59) and (60).

4) Constitutive Laws as Projections: An inclusion cannot be directly employed in numerical calculations. Hence, we transform the force laws (53), (57), and (59) that have been stated as an inclusion to a normal cone, into an equality. This is achieved through the so-called proximal point function $\text{prox}_C(\boldsymbol{x})$, which equals $\boldsymbol{x}$ if $\boldsymbol{x} \in C$ and equals the closest point in C to $\boldsymbol{x}$ if $\boldsymbol{x} \notin C$. The set C must be convex. Using the proximal point function, we transform the force laws into implicit equalities [22]

$$-\gamma_\kappa \in N_{C_\kappa}(\lambda_\kappa) \iff \lambda_\kappa = \text{prox}_{C_\kappa}(\lambda_\kappa - r_\kappa \gamma_\kappa) \quad (61)$$

where $r_\kappa > 0$ for $\kappa = N, T, V$.

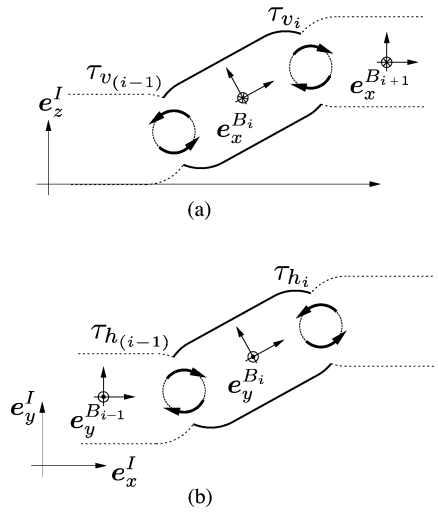

Fig. 5. Control torques. (a) Side view. (b) Top view.

C. Joint Actuators

Each cardan joint has 2 DOF that are controlled by two joint actuators. The actuators are modeled as controlled torques applied around the axes of rotation for the joint. Fig. 5 illustrates how the direction of positive rotation is defined. Define for link i a positive control torque τ_{v_i} to give a positive rotational velocity around $\boldsymbol{e}_x^{B_{i+1}}$ and a positive control torque τ_{h_i} to give a positive rotational velocity around $\boldsymbol{e}_y^{B_i}$, both with respect to link i. The total torque $\boldsymbol{\tau}_{C_i} \in \mathbb{R}^3$ applied to link i is

$$\boldsymbol{\tau}_{C_i} = \begin{bmatrix} 0 \\ \tau_{h_i} \\ 0 \end{bmatrix} - \mathbf{R}_{B_{i-1}}^{B_i} \begin{bmatrix} 0 \\ \tau_{h_{(i-1)}} \\ 0 \end{bmatrix} + \mathbf{R}_{B_{i+1}}^{B_i} \begin{bmatrix} \tau_{v_i} \\ 0 \\ 0 \end{bmatrix} - \begin{bmatrix} \tau_{v_{(i-1)}} \\ 0 \\ 0 \end{bmatrix} \tag{62}$$

for $i = 1, \ldots, n$, where the relative rotation matrix is

$$\mathbf{R}_{B_{i+1}}^{B_i} = \left(\mathbf{R}_{B_i}^I\right)^{\mathrm{T}} \mathbf{R}_{B_{i+1}}^I \tag{63}$$

and $\tau_{h_0} = \tau_{v_0} = \tau_{h_n} = \tau_{v_n} = 0$. The vector of the torques applied to all links $\boldsymbol{\tau}_C \in \mathbb{R}^{6n}$ is

$$\boldsymbol{\tau}_C = [\, \mathbf{0}_{1\times 3} \quad \boldsymbol{\tau}_{C_1}^{\mathrm{T}} \quad \mathbf{0}_{1\times 3} \quad \boldsymbol{\tau}_{C_2}^{\mathrm{T}} \quad \cdots \quad \mathbf{0}_{1\times 3} \quad \boldsymbol{\tau}_{C_n}^{\mathrm{T}} \,]^{\mathrm{T}}. \tag{64}$$

VI. Motion Pattern and Joint Control

In this section, we will define the joint angles and show how to control them for snake robot locomotion.

A. Accessing and Control of Joint Angles

The joint angles are not directly accessible from the nonminimal coordinates, but can be calculated from the relative rotation matrices $\mathbf{R}_{B_{i+1}}^{B_i}$ in (63). Assume that $\mathbf{R}_{B_{i+1}}^{B_i}$ is constructed from successive rotations (Euler angles with the zyx-convention) α_{z_i}, α_{h_i}, and α_{v_i}: $\mathbf{R}_{B_{i+1}}^{B_i} = \mathbf{R}_{\alpha_{z_i}} \mathbf{R}_{\alpha_{h_i}} \mathbf{R}_{\alpha_{v_i}}$. Since we have cardan joints, let $\mathbf{R}_{\alpha_{z_i}} = \mathbf{I}_{3\times 3}$ be the rotation around the $\boldsymbol{e}_z^{B_i}$-axis, and let $\mathbf{R}_{\alpha_{h_i}}$ and $\mathbf{R}_{\alpha_{v_i}}$ describe the rotation around $\boldsymbol{e}_y^{B_i}$ and $\boldsymbol{e}_x^{B_{i+1}}$, respectively. Hence, α_{h_i} describes the DOF of the cardan joint between link i and link $i+1$ that moves link i and $i+1$ from side to side, and α_{v_i} describes the lifting and lowering of the links. The rotation angles can now be found from the relative rotation matrix (63) as

$$\alpha_{v_i} = \tan^{-1}\left[\frac{(\mathbf{R}_{B_{i+1}}^{B_i})_{32}}{(\mathbf{R}_{B_{i+1}}^{B_i})_{33}}\right] \tag{65}$$

$$\alpha_{h_i} = -\sin^{-1}\left(\mathbf{R}_{B_{i+1}}^{B_i}\right)_{31} \tag{66}$$

for $i = 1, \ldots, n-1$, where $(\mathbf{R}_{B_{i+1}}^{B_i})_{32}$ is the element of the matrix $\mathbf{R}_{B_{i+1}}^{B_i}$ in row 3 column 2, etc.

The rotational velocities of the joints are found directly from the rotational velocities of the links. We define the rotational velocity for sideways motion as $\omega_{h_i} = \boldsymbol{d}_2^T \boldsymbol{\omega}_{J_i}$ and lifting motion as $\omega_{v_i} = \boldsymbol{d}_1^T \boldsymbol{\omega}_{J_i}$ for the joint between link i and $i+1$, where $\boldsymbol{d}_1^T = [\,1 \quad 0 \quad 0\,]$, $\boldsymbol{d}_2^T = [\,0 \quad 1 \quad 0\,]$, and

$$\boldsymbol{\omega}_{J_i} = {}_{B_{i+1}}\boldsymbol{\omega}_{IB_{i+1}} - \left(\mathbf{R}_{B_{i+1}}^{B_i}\right)_{B_i}^{\mathrm{T}} \boldsymbol{\omega}_{IB_i}. \tag{67}$$

Let the desired values of α_{h_i} and α_{v_i} be $\alpha_{h_i,r}$ and $\alpha_{v_i,r}$, respectively. In addition, the reference values for the joint velocities $\omega_{h_i}, \omega_{v_i}$ are given by $\dot{\alpha}_{h_i,r}$ and $\dot{\alpha}_{v_i,r}$, respectively. Then, proportional derivative (PD) controllers for the joints are

$$\tau_{h_i} = K_{h_p}\left(\alpha_{h_i} - \alpha_{h_i,r}\right) + K_{h_d}\left(\omega_{h_i} - \dot{\alpha}_{h_i,r}\right) \tag{68}$$

$$\tau_{v_i} = K_{v_p}\left(\alpha_{v_i} - \alpha_{v_i,r}\right) + K_{v_d}\left(\omega_{v_i} - \dot{\alpha}_{v_i,r}\right) \tag{69}$$

for $i = 1, \ldots, n-1$, where K_{h_p}, K_{h_d}, K_{v_p}, and K_{v_d} are positive constants and equal for all i.

B. Motion Pattern and Reference Angles

A general expression for defining some of the most common motion patterns for snake robots is given by

$$\alpha_{h_i,r} = A_h \sin\left(\omega_h t + (i-1)\delta_h\right) + \psi_h \tag{70}$$

$$\alpha_{v_i,r} = A_v \sin\left(\omega_v t + (i-1)\delta_v + \delta_0\right) + \psi_v \tag{71}$$

for $i = 1, \ldots, n-1$, where $\alpha_{h_i,r}$ and $\alpha_{v_i,r}$ are the reference angles for α_{h_i} and α_{v_i}, and A_h, A_v are the amplitude of oscillation, ω_h, ω_v are the angular frequencies, δ_h, δ_v are the phase offsets, and ψ_h, ψ_v are the angle offsets, for the horizontal and vertical waves, respectively [3]. The offset between the vertical and horizontal waves is given by δ_0.

Two motion patterns that biological snakes use have been employed in this paper. The first motion pattern is called "lateral undulation" (also denoted "serpentine crawling") where locomotion is obtained by propagating horizontal waves from the front to the rear of the snake body while exploiting roughness in the terrain and digging its body into the ground. These latter two properties are the motivation for our anisotropic friction model. The second motion pattern is called "sidewinding" and is mainly used by biological snakes moving on uniform surfaces [30]. Parts of the snake are lying relatively stationary on the ground while the rest of the body is lifted and moved forward resulting in a looping movement during locomotion.

VII. Numerical Algorithm—Time Stepping

The numerical solution of the equality of measures is found with an algorithm introduced in [23] (see also [22] and [24]) called the time-stepping method described in the following. The methods applied in Section VII-A and Section VII-B are based on [27], except for the direct calculation of the bilateral contact impulsions that we have introduced.

A. Time Discretization

Let t_l denote the time at time step $l = 1, 2, 3, \ldots$, where the step size is $\Delta t = t_{l+1} - t_l$. Consider the (usually very short) time interval $I = [t_A, t_E]$ and let $t_A = t_l$. Define $\boldsymbol{q}_A = \boldsymbol{q}(t_A)$, $\boldsymbol{u}_A = \boldsymbol{u}(t_A)$ that are admissible with respect to both the unilateral and bilateral constraints, and the unit norm constraint on the Euler parameters. Our goal is now to find $\boldsymbol{q}_E = \boldsymbol{q}(t_E)$. We use the states of the system at the *mid point* $t_M = t_A + (1/2)\Delta t$ of the time interval I to decide which contact points are active (i.e., which links are touching the ground). The coordinates (positions and orientations) at t_M are found from

$$\boldsymbol{q}_M = \boldsymbol{q}_A + \frac{\Delta t}{2}\mathbf{F}(\boldsymbol{q}_M)\boldsymbol{u}_A \tag{72}$$

where we have used the equality $\dot{\boldsymbol{p}} = (1/2)\bar{\mathbf{H}}^{\mathrm{T}}\,{}_{B_i}\boldsymbol{\omega}_{IB_i}$ [26],

$$\mathbf{F}(\boldsymbol{q}_M) = \begin{bmatrix} \mathbf{F}_{H_1} & \mathbf{0}_{7\times 6} & \cdots & \mathbf{0}_{7\times 6} \\ \mathbf{0}_{7\times 6} & \mathbf{F}_{H_2} & \cdots & \vdots \\ \vdots & & \ddots & \mathbf{0}_{7\times 6} \\ \mathbf{0}_{7\times 6} & \cdots & \mathbf{0}_{7\times 6} & \mathbf{F}_{H_n} \end{bmatrix} \tag{73}$$

$$\mathbf{F}_{H_i} = \begin{bmatrix} \mathbf{I}_{3\times 3} & \mathbf{0}_{3\times 3} \\ \mathbf{0}_{4\times 3} & \dfrac{1}{2}\bar{\mathbf{H}}_i^{\mathrm{T}} \end{bmatrix} \in \mathbb{R}^{7\times 6} \tag{74}$$

and $\bar{\mathbf{H}}_i$ is found from (6) by inserting the orientation of link i at time t_M. The approximation of the matrices $\mathbf{W}_\Xi$, where $\Xi = N, T, J, V$, on the time interval I is given as $\mathbf{W}_{\Xi M} := \mathbf{W}_\Xi(\boldsymbol{q}_M)$. The same applies for $\boldsymbol{h}_M := \boldsymbol{h}(\boldsymbol{q}_M, \boldsymbol{u}_A)$. A numerical approximation of the equality of measures (46) over the time interval I can now be written as

$$\mathbf{M}(\boldsymbol{u}_E - \boldsymbol{u}_A) - \boldsymbol{h}_M\Delta t - \boldsymbol{S} - \mathbf{W}_{JM}\,\boldsymbol{P}_J = \boldsymbol{\tau}_C\Delta t \tag{75}$$

where

$$\boldsymbol{S} = \sum_{a\in\mathcal{I}}(\mathbf{W}_{NM})_a\,P_{N_a} + [(\mathbf{W}_{TM})_{2a-1}\;(\mathbf{W}_{TM})_{2a}]\,\boldsymbol{P}_{T_a} + \sum_{a\in\mathcal{I}}[(\mathbf{W}_{VM})_{2a-1}\;(\mathbf{W}_{VM})_{2a}]\,\boldsymbol{P}_{V_a} \tag{76}$$

and P_{N_a}, $\boldsymbol{P}_{T_a}$, $\boldsymbol{P}_{V_a}$, and $\boldsymbol{P}_J$ are the contact impulsions during the time interval I. They consist of forces λ acting *during* I, and possible impulses Λ acting *in* the time interval I. The subscript $_a$ denotes which link the contact impulsions are acting on, and is employed the same way as for the contact impulse measures in (50). To find the positions and orientations $\boldsymbol{q}_E$ at the end of the time interval, we need to solve (75) for $\boldsymbol{u}_E$ and the contact impulsions. The contact impulsions associated with ground contact are found using the prox functions described in Section V-B4 for the set of active contact points $\mathcal{I}$. Hence, the constitutive laws (61) for the ground contact impulsions may now be written as

$$P_{N_a} = \mathrm{prox}_{C_N}\left(P_{N_a} - r_N\gamma_{NE_a}\right) \tag{77}$$

$$\boldsymbol{P}_{T_a} = \mathrm{prox}_{C_T}\left(\boldsymbol{P}_{T_a} - r_T\boldsymbol{\gamma}_{TE_a}\right) \tag{78}$$

$$\boldsymbol{P}_{V_a} = \mathrm{prox}_{C_V}\left(\boldsymbol{P}_{V_a} - r_V\boldsymbol{\gamma}_{VE_a}\right) \tag{79}$$

where $r_N, r_T, r_v > 0$, $a \in \mathcal{I}$, γ_{NE_a} is the ath element of the vector $\boldsymbol{\gamma}_{NE}$, and $\boldsymbol{\gamma}_{TE_a}$, $\boldsymbol{\gamma}_{VE_a}$ are the vectors of the $(2a-1)$th and $2a$th elements of $\boldsymbol{\gamma}_{TE}$ and $\boldsymbol{\gamma}_{VE}$, respectively, and

$$\boldsymbol{\gamma}_{NE} = \boldsymbol{\gamma}_N(\boldsymbol{q}_M, \boldsymbol{u}_E) = \mathbf{W}_{NM}^{\mathrm{T}}\,\boldsymbol{u}_E \tag{80}$$

$$\boldsymbol{\gamma}_{TE} := \boldsymbol{\gamma}_T(\boldsymbol{q}_M, \boldsymbol{u}_E) = \mathbf{W}_{TM}^{\mathrm{T}}\,\boldsymbol{u}_E \tag{81}$$

$$\boldsymbol{\gamma}_{VE} := \boldsymbol{\gamma}_V(\boldsymbol{q}_M, \boldsymbol{u}_E) = \mathbf{W}_{VM}^{\mathrm{T}}\,\boldsymbol{u}_E. \tag{82}$$

The constitutive laws (77)–(82) are valid for completely inelastic impact.

The constraints on the joints are bilateral, and it therefore, holds that $\boldsymbol{\gamma}_{JE} := \boldsymbol{\gamma}_J(\boldsymbol{q}_E, \boldsymbol{u}_E) = \mathbf{W}_{JM}^{\mathrm{T}}\,\boldsymbol{u}_E = \mathbf{0}\,\forall\, t$. This allows us to directly compute the associated contact impulsions $\boldsymbol{P}_J$ by solving (75) for $\boldsymbol{P}_J$ with $\boldsymbol{u}_E = \mathbf{0}$. By solving for $\boldsymbol{P}_J$ and solving (75)–(81), we find that

$$\boldsymbol{q}_E = \boldsymbol{q}_M + \frac{\Delta t}{2}\mathbf{F}(\boldsymbol{q}_M)\boldsymbol{u}_E. \tag{83}$$

B. Solving for the Contact Impulsions

In this section, we show how to calculate the contact impulsions P_{N_a}, $\boldsymbol{P}_{T_a}$, $\boldsymbol{P}_{V_a}$, and $\boldsymbol{P}_J$ in (76) for $a \in \mathcal{I}$. The numerical integration algorithm used in this paper is called a time-stepping method that allows for a simultaneous treatment of both impulsive and nonimpulsive forces during a time step. The frictional contact problem, defined by (75)–(82) and finding $\boldsymbol{P}_J$, needs to be solved for each time step t_l. A modified Newton algorithm [31] has been chosen to solve the nonlinear problem iteratively because of its simplicity. Let the superscript $^{(k)}$ denote the current iteration of the modified Newton algorithm, and initialize all contact impulsions (for active contacts) with the value they had the last time their corresponding contact point was active. Let those that *were* active be initialized with their previous values. Now, the algorithm may be written as follows.

1) Solve

$$\boldsymbol{P}_J^{(k)} = \left(\mathbf{W}_{JM}^{\mathrm{T}}\mathbf{M}^{-1}\mathbf{W}_{JM}^{\mathrm{T}}\right)^{-1} \cdot\left[\mathbf{W}_{JM}^{\mathrm{T}}\boldsymbol{u}_A - \mathbf{W}_{JM}^{\mathrm{T}}\mathbf{M}^{-1}\left(\boldsymbol{h}_M\Delta t + \boldsymbol{S}^{(k)} + \boldsymbol{\tau}_C\Delta t\right)\right] \tag{84}$$

where

$$\boldsymbol{S}^{(k)} = \sum_{a\in\mathcal{I}}(\mathbf{W}_{NM})_a\,P_{N_a}^{(k)} + \sum_{a\in\mathcal{I}}[(\mathbf{W}_{TM})_{2a-1}\;(\mathbf{W}_{TM})_{2a}]\,\boldsymbol{P}_{T_a}^{(k)} + \sum_{a\in\mathcal{I}}[(\mathbf{W}_{VM})_{2a-1}\;(\mathbf{W}_{VM})_{2a}]\,\boldsymbol{P}_{V_a}^{(k)}. \tag{85}$$

2) Solve $\boldsymbol{u}_E^{(k+1)}$ from

$$\mathbf{M}\left(\boldsymbol{u}_E^{(k+1)} - \boldsymbol{u}_A\right) - \boldsymbol{h}_M\,\Delta t - \boldsymbol{S}^{(k)} - \mathbf{W}_{JM}\,\boldsymbol{P}_J^{(k)} = \boldsymbol{\tau}_C\,\Delta t. \tag{86}$$

3) Solve for $a \in \mathcal{I}$

$$\boldsymbol{P}_{N_a}^{(k+1)} = \text{prox}_{C_N}\left(P_{N_a}^{(k)} - r_N \gamma_{NE_a}^{(k+1)}\right) \tag{87}$$

$$\boldsymbol{P}_{T_a}^{(k+1)} = \text{prox}_{C_T}\left(\boldsymbol{P}_{T_a}^{(k)} - r_T \gamma_{TE_a}^{(k+1)}\right) \tag{88}$$

$$\boldsymbol{P}_{V_a}^{(k+1)} = \text{prox}_{C_V}\left(\boldsymbol{P}_{V_a}^{(k)} - r_V \gamma_{VE_a}^{(k+1)}\right) \tag{89}$$

where

$$\boldsymbol{\gamma}_{NE}^{(k+1)} = \mathbf{W}_{NM}^{\mathrm{T}}\,\boldsymbol{u}_E^{(k+1)} \tag{90}$$

$$\boldsymbol{\gamma}_{TE}^{(k+1)} = \mathbf{W}_{TM}^{\mathrm{T}}\,\boldsymbol{u}_E^{(k+1)} \tag{91}$$

$$\boldsymbol{\gamma}_{VE}^{(k+1)} = \mathbf{W}_{VM}^{\mathrm{T}}\,\boldsymbol{u}_E^{(k+1)}. \tag{92}$$

Repeat steps 1)–3) until

$$\left\|\boldsymbol{P}_N^{(k+1)} - \boldsymbol{P}_N^{(k)}\right\| + \left\|\boldsymbol{P}_T^{(k+1)} - \boldsymbol{P}_T^{(k)}\right\| + \left\|\boldsymbol{P}_V^{(k+1)} - \boldsymbol{P}_V^{(k)}\right\| < \epsilon \tag{93}$$

where $\epsilon > 0$ is a user-defined tolerance. Subsequently, $\boldsymbol{q}_E$ is calculated from (83) and the calculation of the time step is finished. Usually, a higher value of the parameters r_N, r_T, r_V yields a faster convergence rate at the risk of divergence. However, a general convergence result for the modified Newton algorithm does not exist. The constitutive laws (87)–(92) used to describe the contact impulses are given on *velocity level*. This means that the bilateral constraints on position level, and the unit norm constraint on the Euler parameters are, in general, not satisfied. A solution to these problems is suggested in the following.

C. Constraint Violation

After the modified Newton algorithm has converged and $\boldsymbol{q}_E$ has been found from (83), the unit-norm constraint $\|\boldsymbol{p}_i\| = 1$ is satisfied from $\boldsymbol{p}_{E_i}^{\text{new}} = \boldsymbol{p}_{E_i}/\|\boldsymbol{p}_{E_i}\|$, for $i = 1, \ldots, n$, where $\boldsymbol{p}_{E_i}$ is the quaternion describing the orientation of link i. The new quaternions should now be inserted into $\boldsymbol{q}_E$.

The links have to be projected so that the bilateral constraints (12), (13) are satisfied. This is done in a two-step process while keeping the position and orientation of link 1 fixed. First, the orientation of the positions of the remaining links are altered so that $g_{J_{i\phi}} = 0$ is satisfied for $i = 1, \ldots, n-1$. In this process, all the $\boldsymbol{e}_z^{B_i}$-axes are kept fixed, while the $\boldsymbol{e}_x^{B_i}$ and $\boldsymbol{e}_y^{B_i}$ are changed, if necessary. Subsequently, the remaining links are translated so that $g_{J_{i\chi}} = 0$ is satisfied for $i = 1, \ldots, n-1$, $\chi = x, y, z$. The new positions of the links should now be inserted into $\boldsymbol{q}_E$. Now, the positions $\boldsymbol{q}_E$ and velocities $\boldsymbol{u}_E$ can be used as the initial states for the next time step t_{l+1}.

VIII. Simulations And Experimental Validation

In this section, we present simulations of the mathematical model together with experiments with a real snake robot. First, we present the model and simulation parameters. Second, simulation results of the motion pattern lateral undulation are given with orthotropic friction. Finally, the latter three sections present the experimental setup together with simulation and experimental results of the motion patterns lateral undulation and sidewinding with isotropic friction.

A. Model and Simulation Parameters

The snake robot Aiko in Fig. 1 was used as a basis for the parameters in the mathematical model. The model parameters are for $i = 1, \ldots, n$: Aiko has $n = 11$ links. The length $L_i = 0.122$ m and radius $L_{SC_i} = 0.0525$ m of each link is found by measuring one of the links used on Aiko. Moreover, Aiko weighs 7.5 kg, and we therefore, assume that each link weighs $m_i = 7.5/11$ kg ≈ 0.682 kg since all links are approximately equal. The distance from the center of gravity of a link to the center of the spheres used for contact with the ground in the model is calculated to be $L_{GS_i} = 0.0393$ m by assuming a 45° maximum joint deflection and that the cylindrical parts of the model should not come into each other for a maximum joint angle. The moments of inertia $\Theta_{1i} = 9.63 \times 10^{-4}$ kg·m^2, $\Theta_{3i} = 2.35 \times 10^{-4}$ kg·m^2 are calculated by assuming each link to be a cylinder of length L_i and radius L_{SC_i} with a uniform mass distribution.

The controller parameters are $K_{h_p} = 40$ Nm, $K_{h_d} = 0.2$ Nm·s, $K_{v_p} = 800$ Nm, and $K_{v_d} = 0.2$ Nm·s. The acceleration of gravity is $g = 9.81$ m/s^2. The simulation parameters are as follows: $r_N = 0.1$, $r_T = 0.01$, $r_V = 0.05$, $t_{\text{start}} = 0$ s, $t_{\text{stop}} = 15$ s, $\Delta t = (t_{\text{stop}} - t_{\text{start}})/N$ seconds, and $N = 4000(t_{\text{stop}} - t_{\text{start}})$. The Coulomb friction coefficients are given together with the presentation of the simulations since we have not employed the same friction coefficients for all simulations.

B. Lateral Undulation: Simulation Results

In this section, we let the snake robot move by the motion pattern lateral undulation (see Section VI). We include this motion pattern since it is commonly used for snake robots [1], [10]–[13], [32]–[34], and we therefore, want to show that the desired (forward) motion is obtained for our model. We do not provide an experimental validation in this section since our snake robot Aiko does not have the orthotropic friction property necessary for efficient locomotion by lateral undulation on a flat surface. However, we compare simulation and experimental results for lateral undulation with *isotropic* friction in Section VIII-D.

The Coulomb friction coefficients $\mu_{T_x} = 0.1$ (along the snake robot body) and $\mu_{T_y} = 0.5$ (transversal to the body) are employed for the simulation of lateral undulation in this section. Hence, orthotropic friction is obtained. The motion pattern is implemented using the joint reference angles given by (70) and (71) with the parameters $A_h = 30\pi/180$ rad, $\omega_h = 80\pi/180$ rad/s, $\delta_h = -50\pi/180$ rad, $A_v = \delta_v = \psi_v = \psi_h = \delta_0 = 0$ rad, and $\omega_v = 0$ rad/s. We let the snake robot start in a curved posture with its center line approximately along the $\boldsymbol{e}_x^I$-axis and with its initial joint angles given by $\alpha_{h_i}(0)$ and $\alpha_{v_i}(0)$, respectively.

Fig. 6 shows the position of the center of gravity of the middle link $(i = 6)$ of the snake robot. We see that the snake robot behaves as expected: the snake robot starts moving steadily

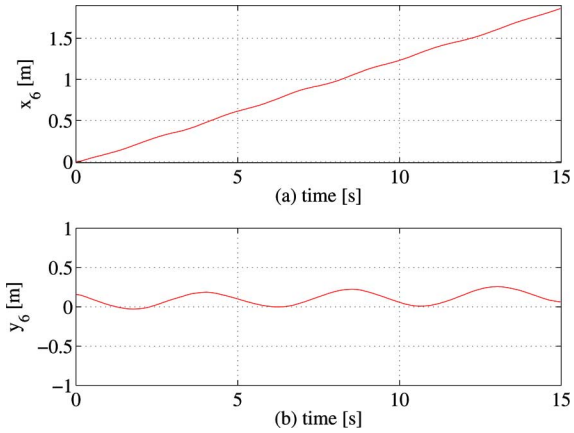

Fig. 6. Simulation results (solid line) of the position (x_6, y_6) of the center of gravity of link 6 in the $(\boldsymbol{e}_x^I, \boldsymbol{e}_y^I)$-plane during lateral undulation. The model is simulated with orthotropic friction.

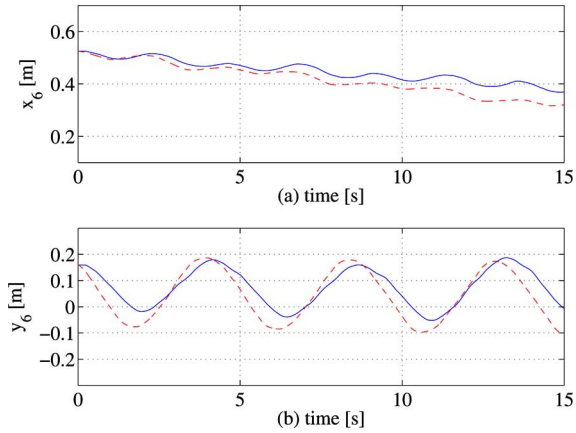

Fig. 7. Position of link 6 during lateral undulation with isotropic friction on a flat plane: simulation (dashed line) and experimental (solid line) results.

forward mainly along the $\boldsymbol{e}_x^I$-axis. The forward motion would not have been the result for an isotropic friction model (i.e., $\mu_{T_x} = \mu_{T_y}$). In that case, the snake robot would have moved slowly backward as we will see in Section VIII-D. In order to increase the velocity of a snake robot, even with isotropic friction, the snake robot may push against external objects to move forward. Such an approach is elaborated on in, e.g., [35] and [36].

C. Experimental Setup

The snake robot Aiko (Fig. 1) used in the experiments was built in 2006 at the NTNU/SINTEF Advanced Robotics Laboratory,[1] Trondheim, Norway. Aiko has ten 2 DOF cardan joints and 11 links. The length L_i and mass m_i of the links are the same as given for the mathematical model in Section VIII-A. The metal sphere used as a "face" in Fig. 1 was removed in the experiments to obtain a uniform weight distribution along the snake robot. The friction coefficients in the model were calculated from the measurements obtained by dragging Aiko from a scale along the particle board. The friction coefficients were found to be $\mu_{T_x} = \mu_{T_y} = 0.2$, and these values will be employed in the simulations in the remainder of this paper.

Each 2 DOF cardan joint was actuated by two 6 W dc motors. The two motors were controlled by a controller with dynamic feedback [37] implemented on an Atmel ATmega128 microcontroller. The snake robot joint reference angles were sent with a frequency of 10 Hz from a PC, via a controller area network (CAN) bus to the microcontrollers. The position of the center of the middle link (link 6) was tracked using a Vicon MX Motion Capture System with four cameras (MX3) together with Matlab Simulink. The Vicon programme (Vicon iQ 2.0) ran on a computer with four Intel Xeon 3 GHz processors and 2 GB RAM. The logging of motion data was synchronized in time through a Transmission Control Protocol (TCP) connection between the PC that controlled Aiko and the Vicon-computer at the startup of the transmission of the desired snake robot joint angles. Data logging was performed at 20 Hz. We have chosen to let the position of link 6 represent the position of the snake robot, because then we filter any transient behavior of the snake robot that might occur at its ends, and it is thus, easier to focus on the general motion of the snake robot. The center of gravity of the whole snake robot (instead of a specific link) can also be advantageous to be used to represent the position of the snake robot. However, such an approach is cumbersome to realize with our Vicon system.

Particle boards were used as the ground surface.

[1]Online Available: http://www.sintef.com/snakerobots

D. Lateral Undulation: Simulation and Experimental Results

In this section, we compare simulation and experimental results for lateral undulation with isotropic friction. The reference joint angles are calculated from (70) and (71) with the parameters $A_h = 40\pi/180$ rad, $\omega_h = 80\pi/180$ rad/s, $\delta_h = -50\pi/180$ rad, $A_v = \delta_v = \delta_0 = 0$ rad, $\omega_v = 0$ rad/s, and $\psi_h = \psi_v = 0$, for both the simulation and the experiment. We let the snake robot start in a curved posture with its center line approximately along the $\boldsymbol{e}_x^I$-axis and with its initial joint angles given by $\alpha_{h_i}(0)$ and $\alpha_{v_i}(0)$. Fig. 7 shows both the position of link 6 calculated from the mathematical model in the simulation and the position logged from the experiment with Aiko. We see that the snake robot moves slowly backward along the $\boldsymbol{e}_x^I$-axis. From Fig. 7, we see that the 3-D model display the same trend in motion as observed in the experiment. However, the distance traveled is greater in the simulation, and we have tried varying the friction coefficients (while still keeping isotropic friction), but this did not seem to have a noticeable effect on the simulation results. The difference in distance traveled may come as a consequence of that the model of the snake robot is able to control its joints more accurately, and thus, is able to reach the maximum amplitude when it is required to do so. Also, this suggests that the friction contact between the snake robot and the ground surface is even more complex than what has been accounted for in the model. A more elaborate list of possible sources of errors is given in Section VIII-F.

We note from these simulation and experimental results that the direction of locomotion by lateral undulation with isotropic

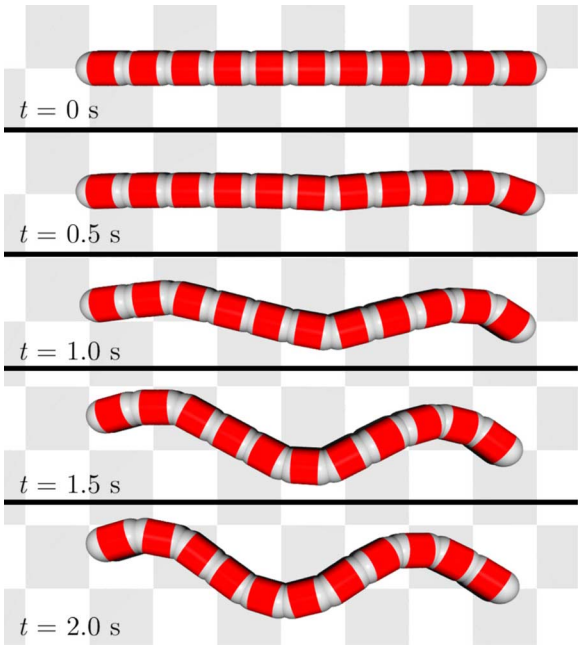

Fig. 8. Top-down view of snake robot postures during simulation of startup with the "soft-start" approach for sidewinding.

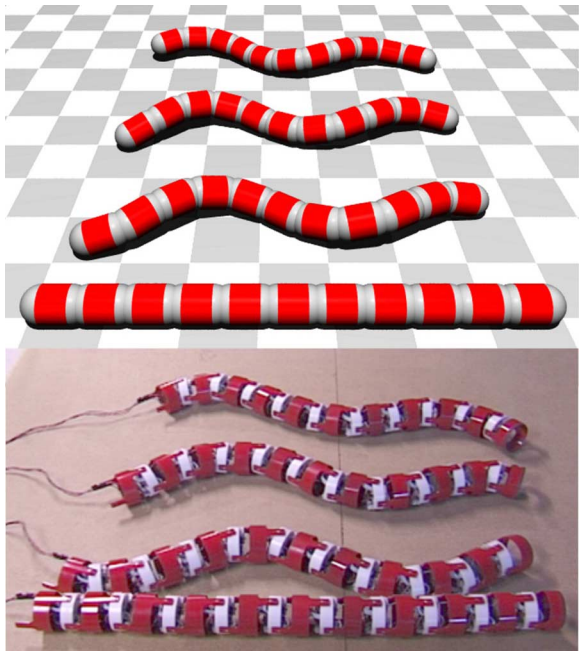

Fig. 9. Aiko (bottom) and simulated snake robot (top) during sidewinding. The images show the snake robot at $t = 0$ s (straight posture), $t = 5$ s, $t = 10$ s, and $t = 15$ s.

friction is the same as the direction of the waves that is propagated along the body of the snake robot. This is coherent with results found in [38], where this phenomenon is elaborated on.

E. Sidewinding: Simulation and Experimental Results

In this section, we present and compare the simulation results and the experimental results for the motion pattern sidewinding. The joint reference angles are found from (70) and (71) with the parameters $A_h = 30\pi/180$ rad, $\omega_h = 80\pi/180$ rad/s, $\delta_h = -50\pi/180$ rad, $A_v = 10\pi/180$ rad, $\omega_v = \omega_h$, $\delta_v = \delta_h$, $\delta_0 = 90\pi/180$ rad, and $\psi_h = \psi_v = 0$ rad, for both the simulation and the experiment. We employ a "soft start" approach during the startup of the snake robot from its initial (straight) posture to avoid large steps in the reference signal. To this end, we override the expressions (70) and (71) and set $\alpha_{h_i}(t) = 0$ rad until the reference signal is within $|\alpha_{h_i}(t)| \leq 3\pi/180$ rad for the first time after startup. The same applies for α_{v_i}. The shape of the snake robot during startup with the "soft-start" approach is illustrated in Fig. 8 for sidewinding.

Fig. 9 illustrates how Aiko and the model move during the 15 s simulation of sidewinding locomotion. Since all the simulations have now been performed, a note on the computational cost is appropriate. All simulations were performed on a Pentium-M 1.8 GHz computer running Matlab R2006a. For 20 s simulations, it took on average about 7.1 min to simulate 1 s of sidewinding motion and only 1.3 min to simulate 1 s of lateral undulation. The difference in simulation speed arises from that the 3-D motion during sidewinding is more complex than planar motion by lateral undulation. The simulation speed can be greatly increased by instead implementing the model in, for example, C++. However, we have chosen to first implement the model in Matlab in order to keep the time it takes to implement the model relatively short.

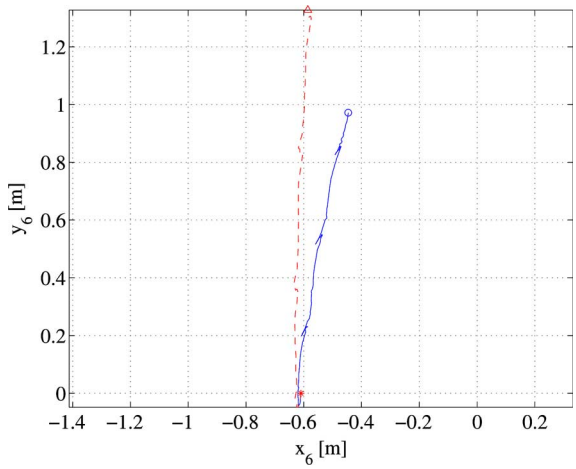

Fig. 10. Position of link 6 during sidewinding on a flat plane: simulation (dashed line) and experimental (solid line) results. The triangle and the circle mark the end of the paths.

Figs. 10 and 11 display the position of link 6 for the 3-D model and Aiko during sidewinding. We observe from the figures that the model almost follows the $\boldsymbol{e}_y^I$-axis, while Aiko steadily turns somewhat to the right. In addition, the model covers a greater distance than Aiko. We see from Figs. 10 and 11(b) that the simulation results have the same trend and approximate frequency as the experimental results along the $\boldsymbol{e}_y^I$-axis. The variance in trend is more noticeable along the $\boldsymbol{e}_x^I$-axis due to the turning motion of Aiko. Moreover, a slight initial difference between the orientation of Aiko and the model may contribute to the discrepancy in heading. We discuss in Section VIII-F various reasons

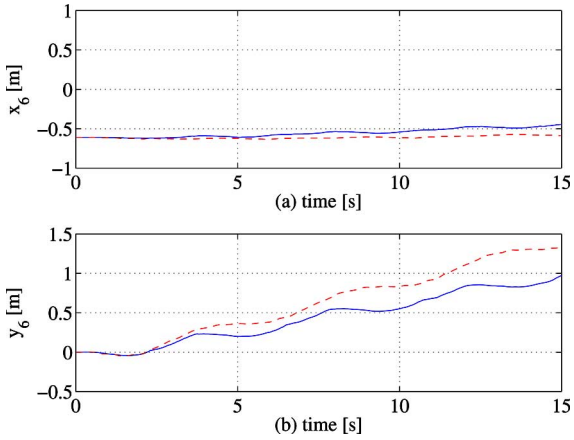

Fig. 11. Position of link 6 during sidewinding on a flat plane:simulation (dashed line) and experimental (solid line) results.

for the differences between the simulation and experimental results. For sidewinding, we believe that one of the most important differences between the 3-D model and Aiko is that Aiko is not able to control its joints accurately. This is particularly the case for vertical (lifting) motion that is needed for sidewinding. By inspecting Aiko closely during the experiment, we noticed that a large part of its body was touching the ground at the same time. This was not the case in the simulation where the snake robot joints were accurately controlled that resulted in that most if its body was lifted from the ground during locomotion.

We observe from Figs. 10 and 11(b) that Aiko sometimes slides a little backward (at $t \approx 5$ s, $t \approx 9$ s, and $t \approx 14$ s). We have tried to reproduce this phenomenon in the 3-D model by lowering and increasing the friction coefficient. We have also tried a variety of anisotropic friction properties, but without any luck. The backward motion might be a result of Aiko not being able to lift its links properly. The links that are supposed to be lifted and moved forward are instead sometimes dragged along the particle board. This results in a friction force that acts in the opposite direction of the desired motion of the snake robot. This friction force might result in that some of the parts that are supposed to be lying stationary on the ground are instead pushed slightly backward.

F. Discussion of the Experimental Validation

We see from Figs. 10 and 11 that the simulation and experimental results compare fairly well. However, the differences between the two results need to be addressed, and we list the most important possible sources of errors in the following. These effects have not been included in the mathematical model.

1) Aiko has a noticeable free play in the joints of about 3–5°. This results in that the control of the joint angles is not completely accurate and a joint angle might not be able to reach its desired angle.
2) The dynamics of the actuators are not modeled. Hence, the actuators in the models are extremely strong and fast, and we are able to accurately control the actual angle of each joint to its desired position. This is not the case for Aiko where the joint motors sometimes saturate and are unable to track the desired joint movement precisely. This particularly the case for vertical motion where larger joint torques are required.
3) The exoskeleton of Aiko is not modeled precisely since this would require a great deal of consideration of the geometry of the snake robot, and this would severely complicate the expressions for contact with the environment.
4) For each cardan joint, there is, in fact, a 2.2 cm distance between the rotational axes for the yaw and pitch motion. However, to simplify the kinematics, we have assumed that the axes intersect.
5) The Stribeck effect [22] is not included in the model of friction. The Stribeck effect states, roughly speaking, that friction forces acting on a body is reduced just after it is set in motion.
6) The varnish on the underside of the snake robot has been worn down. This has resulted in that the snake robot links slide easier when rolled slightly to one of the sides where the varnish is still present.
7) There was a time delay between the startup of the snake robot and the startup of the logging of position data. This delay ranged between 50 and 150 ms.
8) The physical parameters of the snake robot may be slightly incorrect, partly since we assume that each link has a uniform mass distribution.

The list of possible errors is long, and it is difficult to determine what issues are the most important in order to explain the differences between the simulation and experimental results. Also, the main factors may vary depending on which motion pattern is tested. To this end, we believe that for lateral undulation 1) and 2) are the most important reasons for the differences since the snake robot is always lying flat on the ground. Moreover, for sidewinding locomotion, 1)–5) affect the comparison the most.

Even though there are several sources of error, we see from the plots that compare the simulation and experimental results that the model gives a satisfactory qualitative description of the snake robot dynamics. The model is not accurate enough to precisely predict the quantitative motion of the snake robot, but it should be possible to improve the accuracy of the model by taking into account the various sources of errors listed before. However, at its current state, the model gives a clear indication of how the snake robot will move during sidewinding and lateral undulation with isotropic friction and extending the model will require a considerable amount of work in tailoring the model to the specific snake robot Aiko. Hence, the process will have to be repeated for new snake robot designs. Instead of presenting a model with such a very close resemblance to Aiko, we present a model for synthesis and testing of new 3-D motion patterns. Moreover, the comparisons between the simulation and experimental results suggest that our model is valid for this purpose.

IX. Conclusion And Further Work

In this paper, we present a 3-D nonsmooth mathematical model that enables synthesis and testing of 3-D snake robot motion patterns. Experiments show that the models describe in a realistic manner how a real snake robot will behave during locomotion.

The model of the snake robot is developed based on the framework of nonsmooth dynamics and convex analysis. This framework allows us to easily incorporate the contact forces with the ground, together with an accurate description of the spatial Coulomb friction. In addition, even though we employ a hybrid model, there is no need for an explicit switch between system equations (when, for example, an impact occurs) since both the nonimpulsive forces and the impact impulses are covered by the same force law together with that we use the time-stepping method for numerical treatment. The use of nonminimal absolute coordinates results in a constant and diagonal mass matrix and an effective way of writing the system equations. Such a constant mass matrix is beneficial in the numerical treatment since it needs only to be inverted once and not in each time step during simulation.

Simulations of the snake robot during the serpentine motion pattern lateral undulation is performed. The simulation result shows that the orthotropic friction model based on Coulomb's law of dry friction is reasonable since the snake robot moves forward.

Experiments are performed with the snake robot Aiko in Fig. 1 for the serpentine motion patterns lateral undulation and sidewinding with isotropic friction. Back-to-back comparisons between simulation results and experimental results with these motion patterns are given to validate the mathematical model. The simulation and experimental results compare satisfactorily.

The simulation results together with the experimental validation show that the mathematical model presented in this paper gives a satisfactory description of how our snake robot moves in the real world. The model cannot be employed directly (as, e.g., a state estimator) to predict the exact motion of our snake robot. However, the comparisons with experimental results show that the model is suitable for developing and testing motion patterns in order to see how a real snake robot will move for a given motion pattern.

We show in this paper how to develop a 3-D mathematical model of a snake robot on a flat ground surface. Further work will consist of extending the model to include other ground shapes such as stairs. Also, the model will be used to develop and test new 3-D motion patterns for snake robots. Moreover, the optimization of nonsmooth systems is a growing field of research and the 3-D model presented in this paper may, one day, be employed to optimize gaits with respect to, for example, speed or energy efficiency.

It is hoped that this paper can inspire other communities working on robot manipulators to try out the powerful modeling techniques available in the framework of nonsmooth dynamics and convex analysis.

REFERENCES

[1] S. Hirose, *Biologically Inspired Robots: Snake-Like Locomotors and Manipulators*. Oxford, U.K.: Oxford Univ. Press, 1993.

[2] S. Hirose and A. Morishima, "Design and control of a mobile robot with an articulated body," *Int. J. Robot. Res.*, vol. 9, no. 2, pp. 99–114, 1990.

[3] P. Liljebäck, Ø. Stavdahl, and K. Y. Pettersen, "Modular pneumatic snake robot: 3D modelling, implementation and control," presented at the 16th IFAC World Congr., Prague, Czech Republic, Jul. 2005.

[4] M. Mori and S. Hirose, "Three-dimensional serpentine motion and lateral rolling by active cord mechanism ACM-R3," in *Proc. IEEE/RSJ Int. Conf. Intell. Robots Syst.*, 2002, pp. 829–834.

[5] G. Chirikjian and J. Burdick, "Design and experiments with a 30 DOF robot," in *Proc. IEEE Int. Conf. Robot. Autom.*, 1993, vol. 3, pp. 113–119.

[6] G. Chirikjian and J. Burdick, "The kinematics of hyper-redundant robot locomotion," *IEEE Trans. Robot. Autom.*, vol. 11, no. 6, pp. 781–793, Dec. 1995.

[7] S. Ma, Y. Ohmameuda, K. Inoue, and B. Li, "Control of a 3-dimensional snake-like robot," in *Proc. IEEE Int. Conf. Robot. Autom.*, vol. 2, Taipei, Taiwan, Sep. 2003, pp. 2067–2072.

[8] J. Burdick, J. Radford, and G. Chirikjian, "A 'sidewinding' locomotion gait for hyper-redundant robots," in *Proc. IEEE Int. Conf. Robot. Autom.*, May, 1993, pp. 101–106.

[9] A. A. Transeth and K. Y. Pettersen, "Developments in snake robot modeling and locomotion," in *Proc. IEEE Int. Conf. Control, Autom., Robot. Vis.*, Singapore, Dec. 2006, pp. 1393–1400.

[10] S. Ma, N. Tadokoro, B. Li, and K. Inoue, "Analysis of creeping locomotion of a snake robot on a slope," in *Proc. IEEE Int. Conf. Robot. Autom.*, Sep., 2003, pp. 2073–2078.

[11] K. McIsaac and J. Ostrowski, "Motion planning for anguilliform locomotion," *IEEE Trans. Robot. Autom.*, vol. 19, no. 4, pp. 637–625, Aug. 2003.

[12] M. Saito, M. Fukaya, and T. Iwasaki, "Serpentine locomotion with robotic snakes," *IEEE Control Syst. Mag.*, vol. 22, no. 1, pp. 64–81, Feb. 2002.

[13] S. Ma, "Analysis of creeping locomotion of a snake-like robot," *Adv. Robot.*, vol. 15, no. 2, pp. 205–224, 2001.

[14] I. Tanev, T. Ray, and A. Buller, "Automated evolutionary design, robustness, and adaptation of sidewinding locomotion of a simulated snake-like robot," *IEEE Trans. Robot.*, vol. 21, no. 4, pp. 632–645, Aug. 2005.

[15] P. Lamon, T. Thueer, R. Jordi, and R. Siegwart, "Modeling and optimization of wheeled rovers," presented at the 8th ESA Workshop Adv. Space Technol. Robot., New Orleans, LA, 2004.

[16] S. Ma, Y. Ohmameuda, and K. Inoue, "Dynamic analysis of 3-dimensional snake robots," in *Proc. IEEE/RSJ Int. Conf. Intell. Robots Syst.*, 2004, pp. 767–772.

[17] F. Matsuno and H. Sato, "Trajectory tracking control of snake robots based on dynamic model," in *Proc. IEEE Int. Conf. Robot. Autom.*, 2005, pp. 3029–3034.

[18] P. Prautsch, T. Mita, and T. Iwasaki, "Analysis and control of a gait of snake robot," *Trans. Inst. Electr. Eng. J. Ind. Appl. Soc.*, vol. 120-D, pp. 372–381, 2000.

[19] B. Brogliato, *Nonsmooth Mechanics*, 2nd ed. London, U.K.: Springer-Verlag, 1999.

[20] R. Smith. (2007, Nov. 15). Open Dynamics Engine v0.5 user guide [Online]. Available: http://ode.org/ode-latest-userguide.html

[21] Ch. Glocker, *Set-Valued Force Laws, Dynamics of Non-Smooth Systems* (Lecture Notes in Applied Mechanics). vol. 1, Berlin, Germany: Springer-Verlag, 2001.

[22] R. I. Leine and H. Nijmeijer, *Dynamics and Bifurcations of Non-Smooth Mechanical Systems* (Lecture Notes in Applied and Computational Mechanics). vol. 18, Berlin, Germany: Springer-Verlag, 2004.

[23] J. J. Moreau, "Unilateral contact and dry friction in finite freedom dynamics," in *Non-Smooth Mechanics and Applications* (CISM Courses and Lectures), vol. 302, J. J. Moreau and P. D. Panagiotopoulos, Eds., Vienna ed.. Austria: Springer-Verlag, 1988, pp. 1–82.

[24] Ch. Glocker and C. Studer, "Formulation and preparation for numerical evaluation of linear complementarity systems in dynamics," *Multibody Syst. Dyn.*, vol. 13, pp. 447–463, 2005.

[25] A. A. Transeth, R. I. Leine, Christoph Glocker, and K. Y. Pettersen, "Non-smooth 3D modeling of a snake robot with frictional unilateral constraints," in *Proc. IEEE Int. Conf. Robot. Biomimetics*, Kunming, China, Dec. 2006, pp. 1181–1188.

[26] O. Egeland and J.T. Gravdahl, *Modeling and Simulation for Automatic Control*. Trondheim, Norway: Marine Cybernetics, 2002.

[27] C. Le Saux, R. I. Leine, and Ch. Glocker, "Dynamics of a rolling disk in the presence of dry friction," *J. Nonlinear Sci.*, vol. 15, no. 1, pp. 27–61, 2005.

[28] R. T. Rockafellar, *Convex Analysis* (Princeton Landmarks in Mathematics). Princeton, NJ: Princeton Univ. Press, 1970.

[29] A. A. Transeth, R. I. Leine, Ch. Glocker, and K. Y. Pettersen, "Non-smooth 3D modeling of a snake robot with external obstacles," in *Proc. IEEE Int. Conf. Robot. Biomimetics*, Kunminga, China, Dec. 2006, pp. 1189–1196.

[30] J. Gray, "The mechanism of locomotion in snakes," *J. Exp. Biol.*, vol. 23, no. 2, pp. 101–120, 1946.

[31] P. Alart and A. Curnier, "A mixed formulation for frictional contact problems prone to Newton like solution methods," *Comput. Methods Appl. Mech. Eng.*, vol. 92, pp. 353–375, 1991.
[32] J. Ostrowski and J. Burdick, "Gait kinematics for a serpentine robot," in *Proc. IEEE Int. Conf. Robot. Autom.*, Apr., 1996, vol. 2, pp. 1294–1299.
[33] P. Wiriyacharoensunthorn and S. Laowattana, "Analysis and design of a multi-link mobile robot (serpentine)," in *Proc. IEEE Int. Conf. Robot., Intell. Syst. Signal Process.*, Dec., 2002, vol. 2, pp. 694–699.
[34] C. Ye, S. Ma, B. Li, and Y. Wang, "Turning and side motion of snake-like robot," in *Proc. IEEE Int. Conf. Robot. Autom.*, 2004, vol. 5, pp. 5075–5080.
[35] Z. Y. Bayraktaroglu, A. Kilicarslan, A. Kuzucu, V. Hugel, and P. Blazevic, "Design and control of biologically inspired wheel-less snake-like robot," in *Proc. IEEE/RAS-EMBS Int. Conf. Biomed. Robot. Biomechatron.*, Feb., 2006, pp. 1001–1006.
[36] A. A. Transeth, R. I. Leine, C. Glocker, K. Y. Pettersen, and P. Liljebäck, "Snake robot obstacle aided locomotion: Modeling, simulations, and experiments," *IEEE Trans. Robot.*, vol. 24, no. 1, pp. 88–104, Feb. 2008.
[37] O. Egeland, *Servo Engineering* (in Norwegian). Trondheim, Norway: Tapir, 1993.
[38] M. Nilsson, "Serpentine locomotion on surfaces with uniform friction," in *Proc. IEEE/RSJ Int. Conf. Intell. Robots Syst.*, 2004, pp. 1751–1755.

Aksel A. Transeth (S'04–M'08) received the M.Sc. and Ph.D. degrees from the Department of Engineering Cybernetics, Norwegian University of Science and Technology (NTNU), Trondheim, Norway, in 2004 and 2008, respectively.

He is currently a Research Scientist in the Department of Applied Cybernetics, SINTEF Information and Communication Technology (ICT), Trondheim, a Norwegian research organization. His current research interests include modeling and control of dynamical systems, biologically inspired locomotion, and robotics.

Remco I. Leine received the M.Sc. degree in mechanical engineering from the Technical University, Delft, Delft, The Netherlands, in 1996, and the Ph.D. degree in mechanical engineering from the Technical University Eindhoven, Eindhoven, The Netherlands, in 2000.

He has been a Postdoctoral Researcher with the Technical University Munich and the Institut National de Recherche en Informatique et en Automatique (INRIA) Rhône-Alpes. He has also been a Postdoctoral Researcher at the Eidgenössische Technische Hochschule (ETH) Zürich, Zurich, Switzerland, where, since 2003, he was a Senior Lecturer in the Institute of Mechanical Systems, and in 2007, obtained his Habilitation and was appointed as a "Privatdozent" of mechanics at the Institut für Mechanische Systeme (IMES) Centre of Mechanics. His current research interests include the intersection of nonsmooth dynamics and nonlinear dynamics: stability theory for nonsmooth systems, friction-induced vibration and nonlinear phenomena, discontinuous bifurcations in nonsmooth dynamical systems, and multibody systems with impact and friction.

Christoph Glocker received the Diploma and the Doctoral degree in mechanical engineering, and the Certificate of Habilitation in mechanics from the Technische Universität (TU) München, Munchen, Germany, in 1989, 1995, and 2001, respectively.

In 1996, he was granted a Feodor Lynen Fellowship supported by the Alexander von Humboldt Foundation and spent one year at Aristotle University of Thessaloniki. In 1997, he joined the TU München as a Senior Engineer. He then joined the Eidgenössische Technische Hochschule (ETH) Zürich, Zurich, Switzerland, where he is currently a Full Professor of mechanics with the Institut für Mechanische Systeme (IMES) Centre of Mechanics. He is engaged in the research of nonsmooth dynamics of mechanical systems with finite degrees of freedom that includes, for example, the friction and impact problem in multibody systems, providing a generalization of classical analytical mechanics. His current research interests also include both theoretical and practical questions concerning the mechanical modeling, the mathematical formulation, and the numerical treatment of systems with discontinuities, as well as their applications to industrial problems.

Kristin Y. Pettersen (S'93–M'98–SM'04) received the M.Sc. and Ph.D. degrees in electrical engineering from the Norwegian University of Science and Technology (NTNU), Trondheim, Norway, in 1992 and 1996, respectively.

She is currently with the Department of Engineering Cybernetics, NTNU, where she became an Associate Professor in 1996 and a Professor in 2002. During 1999, she was a Visiting Fellow in the Department of Mechanical and Aerospace Engineering, Princeton University, Princeton, NJ. She is the author or coauthor of more than 80 published conference and journal papers. Her current research interests include nonlinear control of mechanical systems with applications to robotics, satellites, autonomous underwater vehicles (AUVs), and ships.

Prof. Pettersen received the IEEE Transactions on Control Systems Technology Outstanding Paper Award in 2006. She also holds several board positions.